Integrative single cell and spatial transcriptomic analysis reveal reciprocal microglia-plasma cell crosstalk in the mouse brain during chronic *Trypanosoma brucei* infection

Juan F. Quintana[1,2†], Praveena Chandrasegaran[1,2], Matthew C. Sinton[1,2], Emma Briggs[3], Thomas D. Otto[1,4], Rhiannon Heslop[1,2], Calum Bentley-Abbot[1,2], Colin Loney[5,4], Luis de Lecea[6], Neil A. Mabbott[7], Annette MacLeod[1,2]

[1]Wellcome Centre for Integrative Parasitology (WCIP). University of Glasgow, Glasgow, UK.

[2]Institute of Biodiversity, Animal Health, and Comparative Medicine (IBAHCM), MVLS, University of Glasgow, Glasgow UK.

[3]Institute for Immunology and Infection Research, School of Biological Sciences, University of Edinburgh, Edinburgh, UK.

[4]Institute of Infection, Immunity & Inflammation, MVLS, University of Glasgow, Glasgow, UK.

[5]MRC Centre for Virus Research. University of Glasgow, Glasgow, UK.

[6]Stanford University School of Medicine, Stanford, CA, United States.

[7]The Roslin Institute and Royal (Dick) School of Veterinary Studies, University of Edinburgh, Edinburgh, UK.

[†]Corresponding authors: juan.quintana@glasgow.ac.uk

Keywords: sleeping sickness, African trypanosomes, neuroinflammation, spatial transcriptomics, single cell RNA sequencing, microglia, plasma cells.

Running title: Spatial transcriptomics analysis of the murine forebrain during chronic *T. brucei* infection

Abstract

Human African trypanosomiasis, or sleeping sickness, is caused by the protozoan parasite *Trypanosoma brucei* and induces profound reactivity of glial cells and neuroinflammation when the parasites colonise the central nervous system. However, the transcriptional and functional responses of the brain to chronic *T. brucei* infection remain poorly understood. By integrating single cell and spatial transcriptomics of the mouse brain, we identified that glial responses triggered by infection are readily detected in the proximity to the circumventricular organs, including the lateral and 3rd ventricle. This coincides with the spatial localisation of both slender and stumpy forms of *T. brucei*. Furthermore, *in silico* predictions and functional validations led us to identify a previously unknown crosstalk between homeostatic *Cx3cr1*$^{+}$ microglia and *Cd138*$^{+}$ plasma cells mediated by IL-10 and B cell activating factor (BAFF) signalling. This study provides important insights and resources to improve understanding of the molecular and cellular responses in the brain during infection with African trypanosomes.

Introduction

Chronic infection with *Trypanosoma brucei*, the causative agent of Human African trypanosomiasis (HAT) or sleeping sickness, is associated with extensive and debilitating neuroinflammation (Barrett et al., 2008; Fèvre et al., 2008; Lundkvist et al., 2004; Maclean et al., 2012). Widespread glial cell activation in the CNS, measured by ionized calcium-binding adapter molecule 1 (IBA1) and glial fibrillary acidic protein (GFAP) reactivity, has also been reported in both human brain biopsies and in murine models of infection (Barrett et al., 2008; Etet et al., 2012; Laperchia et al., 2016; Maclean et al., 2012). There is also extensive infiltration of adaptive immune cells that are thought to be critical mediators of the neuroinflammation induced when the parasites colonise the CNS (Laperchia et al., 2016; Olivera et al., 2021). However, an in-depth characterisation of the transcriptional responses to infection, in particular that of innate immune cells in the CNS, is lacking.

The application of single cell RNA sequencing (scRNAseq) has been transformative to understanding brain pathologies such as Alzheimer's disease and has also been recently applied to understand immunological responses to viral infections (Jiang et al., 2020; Mathys et al., 2019; Stephenson et al., 2021; Wang et al., 2021a). Nevertheless, a major limitation of scRNAseq is that it cannot preserve the spatial distribution in the tissue of origin. The integration of scRNAseq with spatial transcriptomics enable us to characterise cellular and tissue responses to infections on regional and global scales. This has been successfully applied to characterise local immune responses to *Mycobacterium tuberculosis* (Carow et al., 2019) and *M. leprae* (Ma et al., 2021) and in the heart during viral myocarditis (Mantri et al., 2021). However, to our knowledge, similar approaches have not been implemented to study tissue responses to protozoan parasites. Here, we present a spatially resolved single cell atlas of the murine CNS in response to *T. brucei*. This integrative approach led us to identify that glia responses triggered by infection are not limited to the hypothalamus but can also be readily detected in close proximity to the circumventricular organs (CVOs), coinciding with the localisation of slender and stumpy forms of *T. brucei*. Furthermore, we identified a previously unknown interaction between homeostatic *Cx3cr1*$^{+}$ microglia and *Cd138*$^{+}$ plasma cells mediated by IL-10 and B cell activating factor (BAFF) signalling. Our spatiotemporal atlas offers novel insights into the interaction between the innate and adaptive immunity during chronic CNS infections and represents a resource to improve our understanding of the molecular and cellular responses triggered in the brain upon infection.

110 **Materials and methods**

111 **Ethical statement.** All animal experiments were approved by the University of Glasgow
112 Ethical Review Committee and performed in accordance with the home office guidelines,
113 UK Animals (Scientific Procedures) Act, 1986 and EU directive 2010/63/EU. All
114 experiments were conducted under SAPO regulations and UK Home Office project licence
115 number PC8C3B25C to Dr. Jean Rodger. The *in vivo* work related to the single cell and
116 spatial transcriptomic experiments were conducted at 25- and 45-days post-infection (dpi)
117 and correlated with increased clinical scores and procedural severity. Subsequent *in vivo*
118 experiments for experimental validation (flow cytometry and imaging) were terminated
119 earlier in line with ethical recommendations from the veterinary team at the University of
120 Glasgow.

121 **Cell lines and *in vitro* culture.** Murine microglia cell line BV2 (kindly gifted by Dr. Marieke
122 Pingen, University of Glasgow) were cultured in DMEM medium (Sigma) supplemented with
123 10% foetal bovine serum (FBS) (Sigma) and 1000 IU/mL penicillin, and 100 mg/ml
124 streptomycin. Cells were maintained at 37°C and 5% CO_2. All of the experiments presented
125 in this study were conducted with cells between passages 3 to 6. We challenged BV2 cells
126 with *Escherichia coli* B55:O5 LPS (Sigma) for a period of 2 hours to trigger an initial pro-
127 inflammatory response, and then incubated these cells with either untreated B cell
128 supernatant, or B cell supernatant pre-treated with a recombinant antibody to deplete IL-10
129 (IgG2b, clone JES5-16E3, Biolegend). As controls, BV2 cells were left untreated or were
130 incubated with *E. coli* LPS.

131 **Gene expression analysis by qRT-PCR.** Total RNA from BV2 murine microglia cell lines
132 was extracted using RNeasy Kit (Qiagen), eluted in 30 μl of nuclease-free water (Qiagen),
133 and quantified using Qubit broad range RNA assay (Invitrogen). qRT-PCR analysis was
134 carried out using the Luna Universal One-Step RT-qPCR kit (NEB) using 100 ng RNA as
135 input according to the manufacturer's protocol, using the primers listed below. For each
136 sample, two technical replicates were included, as well as a nuclease-free water sample as
137 a "no template sample" control to determine background signal. The relative expression was
138 calculated using the $2^{-\Delta\Delta Ct}$ formula, where ΔΔCt represents the normalized Ct value of the
139 target RNA relative to the 18S rRNA and compared to naïve controls. Statistical analysis
140 was conducted using the Mann-Whitney test and p values <0.05 were considered
141 statistically significant.

142

List of primers used for RT-qPCR (all probes against *M. musculus* sequences)			
Target	**Sequence**	**Length (nt)**	**Melting temperature (°C)**
18S forward	TGTGCCGCTAGAGGTGAAATT	21	57.9
18S reverse	TGGCAAATGCTTTCGCTTT	19	52.4
IL-1β forward	CCACAGACCTTCCAGGAGAATG	22	62.1
IL-1β reverse	GTGCAGTTCAGTGATCGTACAGG	23	62.4
TNFα forward	ATGAGCACTGAAAGCATGATCC	22	58.4
TNFα reverse	GAGGGCTGATTAGAGAGAGGTC	22	62.1

Murine infections with *Trypanosoma brucei*. Six to eight week old female C57Black/6J mice (JAX, stock 000664) were inoculated by intra-peritoneal injection with ~2 x 10^3 parasites of strain *T. brucei brucei* Antat 1.1E (Le Ray et al., 1977). Parasitaemia was monitored by regular sampling from tail venesection and examined using phase microscopy and the rapid "matching" method (Herbert and Lumsden, 1976). Uninfected mice of the same strain, sex and age served as uninfected controls. Mice were fed *ad libitum* and kept on a 12 h light–dark cycle. All the experiments were conducted between 8h and 12h. For sample collection, we focussed on the onset of the CNS stage (25 days post-infection) and the onset of neurological symptoms (>30 days post-infection), defined in this study as altered gait, reduced co-ordination of hind limbs, and flaccid and/or intermittent paralysis in at least one hind limb.

Brain slice preparation for hypothalamus single-cell RNA sequencing

Tissue processing and preparation of single cell suspension. Single-cell dissociations for scRNAseq experiments were performed as follow. Animals were infected for 25 and 45 days (*n* = 2 mice / time point), after which hypothalami were harvested for preparation of single cell suspensions. Uninfected animals were also included as naive controls (*n* = 2 mice). Briefly, all mice were killed by rapid decapitation following isoflurane anaesthesia, within the same time (between 8:00 and 10:00 AM). Using a rodent brain slicer matrix (Zivic Instrument), we generated ~150 µm coronal brain sections around the hypothalamic area (bregma −1.34 mm to −1.82 mm, including anterior and posterior hypothalamic structures). The hypothalami were then rapidly excised under a dissection microscope, and the excised hypothalami were then enzyme-treated for ~30 min at 37 °C using protease XXIII (2.5 mg/ml; Sigma) and DNAse I (1 mg/ml; Sigma) in Hank's Balanced Salt Solution (HSBB) (Invitrogen). Slices were washed three times with cold dissociation solution then transferred to a trypsin inhibitor/bovine serum albumin (BSA) solution (1 mg/ml; Sigma) in cold HBSS

169 (Invitrogen). Single-cell suspensions were passed through 70 µm nylon mesh filters to
170 remove any cell aggregates, diluted to ~1,000 cells/µl (in 1X phosphate buffered saline
171 (PBS) supplemented with 0.04% BSA), and kept on ice until single-cell capture using. In
172 parallel, a fraction of these samples was analysed by flow cytometry to estimate the relative
173 proportion of various glial cell types in the single cell suspensions (**S1A Figure**).
174 The single cell suspensions were loaded onto independent single channels of a
175 Chromium Controller (10X Genomics) single-cell platform. Briefly, ~20,000 single cells were
176 loaded for capture using 10X Chromium NextGEM Single cell 3 Reagent kit v3.1 (10X
177 Genomics). Following capture and lysis, complementary DNA was synthesized and
178 amplified (12 cycles) as per the manufacturer's protocol (10X Genomics). The final library
179 preparation was carried out as recommended by the manufacturer with a total of 14 cycles
180 of amplification. The amplified cDNA was used as input to construct an Illumina sequencing
181 library and sequenced on Nextseq 500 and Novaseq 6000 sequencers by Glasgow
182 polyomics.
183 **Read mapping, data processing, and integration.** For FASTQ generation and
184 alignments, Illumina basecall files (*.bcl) were converted to FASTQs using bcl2fastq. Gene
185 counts were generated using Cellranger v.6.0.0 pipeline against a combined *Mus musculus*
186 (mm10) and *Trypanosoma brucei* (TREU927) transcriptome reference. After alignment,
187 reads were grouped based on barcode sequences and demultiplexed using the Unique
188 Molecular Identifiers (UMIs). The mouse-specific digital expression matrices (DEMs) from
189 all six samples were processed using the R (v4.1.0) package Seurat v4.1.0 (Stuart et al.,
190 2019). Additional packages used for scRNAseq analysis included dplyr v1.0.7 (Wickham et
191 al., 2022), RColorBrewer v1.1.2 (http://colorbrewer.org), ggplot v3.3.5 (Wickham, 2016),
192 and sctransform v0.3.3 (Choudhary and Satija, 2022). We initially captured 25,852 cells
193 mapping specifically against the *M. musculus* genome across all conditions and biological
194 replicates, with an average of 37,324 reads/cell and a median of ~587 genes/cell (**Table**
195 **S2A**). The number of UMIs was then counted for each gene in each cell to generate the
196 digital expression matrix (DEM) (Figure S1B). Low quality cells were identified according to
197 the following criteria and filtered out: *i*) nFeature < 200 or >1,500, *ii*) nCounts < 200 or
198 >5,000, *iii*) > 10% reads mapping to mitochondrial genes, and *iv*) > 40% reads mapping to
199 ribosomal genes, v) genes detected < 3 cells. After applying this cut-off, we obtained a total
200 of 13,195 high quality mouse-specific cells with an average of 12,162 reads/cells and a
201 median of 565 genes/cell (S2A Table).

202 We noted that the overall number of UMIs was significantly higher in samples from
203 25 and 45dpi compared to naïve controls (**Figure S1B**). A closer examination of the number
204 of genes/UMIs per cell type enabled us to determine that the overall increase in infected
205 samples derived mostly from microglia and Oligodendrocytes/B cells (**Figure S1B**) and may
206 be indicative of a "transcriptional burst" associated with cell activation. Based on these
207 observations, we considered this differential feature and gene counts when scaling the data
208 (see below). The gene counts for each cell were divided by the total gene counts for the cell
209 and multiplied by the scale factor 10,000. Then, natural-log transformation was applied to
210 the counts. To identify gene signatures that represent outliers we employed two
211 independent but complementary approaches: *i*) The Seurat *FindVariableFeatures* function
212 with default parameters, using vst as selection method, and *ii*) The *plotHighestExprs* in
213 *Scater* package (McCarthy et al., 2017) with default parameters, which led us to identify
214 additional highly variable genes such as pseudogenes and long non-coding RNAs such as
215 *Malat1*. High-quality cells were then normalised using the *SCTransform* function, regressing
216 out for total UMI and genes counts, cell cycle genes, and highly variable genes identified by
217 both Seurat and Scater packages, followed by data integration using *IntegrateData* and
218 *FindIntegrationAnchors*. For this, the number of principal components were chosen using
219 the elbow point in a plot ranking principal components and the percentage of variance
220 explained (10 dimensions) using a total of 5,000 genes, and SCT as normalisation method.
221 In parallel, given the gene/UMIs discrepancies between experimental groups, we analysed
222 the integrated dataset using the STACAS workflow (Andreatta and Carmona, 2021) with
223 default parameters (10 dimensions) to determine if the clusters identified with the Seurat
224 package can be reproduced by an independent method. Overall, we detected the same
225 marker genes and cell types identified by the *IntegrateData* and *FindIntegrationAnchors*
226 function in Seurat (**Table S2D**). We applied the same approach with the myeloid subset with
227 similar results, suggesting that the differential gene/UMI counts between experimental
228 groups (and accounted for when scaling the data) does not cofound downstream detection
229 of marker genes or cell types.
230 **Cluster analysis, marker gene identification, and subclustering.** The integrated dataset
231 was then analysed using *RunUMAP* (10 dimensions), followed by *FindNeighbors* (10
232 dimensions, reduction = "pca") and *FindClusters* (resolution = 0.4). With this approach, we
233 identified a total of 11 cell clusters The cluster markers were then found using the
234 *FindAllMarkers* function (logfc.threshold = 0.25, assay = "RNA"). To identify cell identity
235 confidently, we employed a hierarchical approach, combining unsupervised and supervised

236 cell identity methods. For the unsupervised approach, we implemented two complementary
237 R packages, *scCATCH* (Shao et al., 2020) and *SingleR* (Aran et al., 2019), using
238 hypothalamic datasets built-in as references with default parameters (**Table S2C**). These
239 packages map a query dataset against selected reference atlases, scoring the level of
240 confidence for cell annotation. Cell identities were assigned based on confidence scores
241 and/or independent cell identity assignment by the two packages. Confidence scores >85%
242 were assumed to be reliable and the cell annotations were kept. When the two packages
243 failed to detect cell identity confidently (confidence scores <85% by at least one package),
244 we employed a supervised approach. This required the manual inspection of the marker
245 gene list followed by and assignment of cell identity based on the expression of putative
246 marker genes expressed in the unidentified clusters. This was particularly relevant for
247 immune cells detected in our dataset that were not found in the reference atlases used for
248 mapping. A cluster name denoted by a single marker gene indicates that the chosen
249 candidate gene is selectively and robustly expressed by a single cell cluster and is sufficient
250 to define that cluster (e.g., *Cd79a, Cd8a, C1qa, Cldn5*, among others). The addition of a
251 second marker was used to indicate a secondary identifier that is also strongly expressed
252 in the cluster but shared by two or more subclusters (e.g., *Apoe, Gfap*).
253 When manually inspecting the gene markers for the final cell types identified in our
254 dataset, we noted the co-occurrence of genes that could discriminate two or more cell types
255 (e.g., macrophages from microglia). To increase the resolution of our clusters to help
256 resolve potential mixed cell populations embedded within a single cluster and, we subset
257 vascular associated cells (endothelial cells, pericytes, tanycytes, and ependymocytes),
258 microglia, T cells, and oligodendrocytes (the latter also containing a distinctive B cell cluster)
259 and analysed them individually using the same functions described above. In all cases, upon
260 subsetting, the resulting objects were reprocessed using the functions
261 *FindVariableFeatures, RunUMAP, FindNeighbors*, and *FindClusters* with default
262 parameters. The number of dimensions used in each cased varied depending on the cell
263 type being analysed but ranged between 5 and 10 dimensions. Cell type-level differential
264 expression analysis between experimental conditions was conducted using the
265 *FindMarkers* function (*min.pct* = 0.25, *test.use* = Wilcox) and (*DefaultAssay* = "SCT"). Where
266 indicated, the *AddModuleScore* function was used to assign scores to groups of genes of
267 interest (*Ctrl* = 100, *seed* = NULL, *pool* =NULL), and the scores were then represented in
268 violin plots. This tool measures the average expression levels of a set of genes, subtracted

269 by the average expression of randomly selected control genes. Statistical tests using the
270 non-parametric Wilcox test comparing mean of normalised gene expression (basemean)
271 was conducted in R. Cell-cell interaction analysis mediated by ligand-receptor expression
272 level was conducted using NicheNet (Browaeys et al., 2020) with default parameters using
273 "mouse" as a reference organism, comparing differentially expressed genes between
274 experimental conditions (*condition_oi* = "Infected", *condition_reference* = "Uninfected").
275 Pathways analysis for mouse genes were conducted using STRING (Szklarczyk et al.,
276 2019) with default parameters. Raw data and scripts used for data analysis will be made
277 publicly available after peer review.

278 **10X Visium spatial sequencing library preparation and analysis**

279 **Tissue processing and library preparation.** Coronal brain sections (bregma −1.34 mm to
280 −1.82 mm) were frozen in optimal cutting temperature medium (OCT) and stored at −80 °C
281 until sectioning. Optimization of tissue permeabilization was performed on 10-µm-thick
282 sections using the Visium Spatial Tissue Optimization Reagents Kit (10X Genomics), which
283 established an optimal permeabilization time of 18 min. Samples were mounted onto a Gene
284 Expression slide (10X Genomics) and stored at −80 °C until haematoxylin and eosin (H&E)
285 staining. To prepare for staining, the slide was placed on a thermocycler adaptor set at 37
286 °C for 5 min followed by fixation in ice-cold methanol for 30 min. Methanol was displaced
287 with isopropanol and the samples were air-dried for 5-10 min before sequential staining with
288 Mayer's haematoxylin Solution (Sigma-Aldrich), Bluing Buffer (Dako) and 1:10 dilution of
289 Eosin Y solution (Sigma-Aldrich) in 0.45 M of Tris-acetic acid buffer, pH 6.0, with thorough
290 washing in ultrapure water between each step. Stained slides were scanned under a
291 microscope (EVOS M5000, Thermo). Tissue permeabilization was performed to release the
292 poly-A mRNA for capture by the poly(dT) primers that were precoated on the slide, including
293 a spatial barcode and a Unique Molecular Identifiers (UMIs). The Visium Spatial Gene
294 Expression Reagent Kit (10X Genomics) was used for reverse transcription and second
295 strand synthesis, followed by denaturation, to allow the transfer of the cDNA from the slide
296 to a collection tube. These cDNA fragments were then used to construct spatially barcoded
297 Illumina-compatible libraries using the dual Index Kit TT Set A (10x Genomics) was used to
298 add unique i7 and i5 sample indexes, enabling the spatial and UMI barcoding. The final
299 Illumina-compatible sequencing library was sequenced on a single lane (2x150) of a
300 NextSeq instrument (Illumina) by Glasgow Polyomics.

301 After sequencing, the FASTQ files were aligned to a merged reference transcriptome
302 combining the *Mus musculus* genome (mm10) genome and the *Trypanosome brucei*

303 reference genome (TREU927). After alignment, reads were grouped based on spatial
304 barcode sequences and demultiplexed using the UMIs, using the SpaceRanger pipeline
305 version 1.2.2 (10X Genomics). Downstream analyses of the expression matrices were
306 conducted using the Seurat pipeline for spatial RNA integration (Hao et al., 2021b; Stuart et
307 al., 2019) (**Table S3A**). Specifically, the data was scaled using the *SCTransform* function
308 with default parameters. We then proceeded with dimensionality reduction and clustering
309 analysis using *RunPCA* (*assay* = "SCT"), *FindNeighbours* and *FindClusters* functions with
310 default settings and a total of 30 dimensions. We then applied the *FindSpatiallyVariables*
311 function to identify spatially variable genes, using the top 1,000 most variable genes and
312 "markvariogram" as selection method. We optimised the parameters to obtain clustering of
313 distinct spatially variable gene sets that broadly coincide with several brain regions,
314 including cortex, hippocampus, 3rd and lateral ventricles, thalamus, hypothalamus, striatum,
315 and amygdala (**Materials and Methods, Figure S3**), confirming the robustness,
316 reproducibility, and reliability of our data. For the analysis of the *T. brucei* genes detected in
317 the spatial transcriptomics dataset, we used the *SpatialFeaturePlot* function (*alpha* = 0.01,
318 0.1, *min.cutoff* = 0.1). The genes detected in the spatial transcriptomics dataset at 45dpi
319 where further analysed using the gene ontology server built in the TriTrypDB website (Aslett
320 et al., 2009) with default settings.

321 To integrate our hypothalamic scRNAseq with the 10X Visium dataset, we used the
322 *FindTransferAnchors* function with default parameters, using SCT as normalization method.
323 Then, the *TransferData* function (*weight.reduction* = "pca", 30 dimensions) was used to
324 annotate brain regions based on transferred anchors from the scRNAseq reference
325 datasets. To predict the cell-cell communication mediated by ligand-receptor co-expression
326 patterns in the spatial context, we employed NICHES v0.0.2 (Raredon et al., 2022). Upon
327 dimensionality reduction and data normalisation, NICHES was run using fanton5 as ligand-
328 receptor database with default parameters. The resulting object was then scaled using the
329 functions *ScaleData, FindVariableFeatures* (*selection.method* = "disp"), *RunUMAP* with
330 default settings and a total of 15 dimensions. Spatially resolved expression of ligand-
331 receptor pairs was then identified using the *FindAllMarkers* function (*min.pct* = 0.25, *test.use*
332 = "roc"). For visualisation, we used the *SpatialFeaturePlot* function with default parameters
333 and *min.cutoff* = "q1". Raw data and scripts used for data analysis will be made publicly
334 available after peer review.

335 **Immunofluorescence and single molecule fluorescence *in situ* hybridisation**
336 **(smFISH) using RNAscope.** Formalin-fixed paraffin embedded coronal brain sections were

337 section on a microtome (Thermo) and fixed in 4% PFA for 10 min at room temperature.
338 Sections were blocked with blocking buffer (1X PBS supplemented with 5% foetal calf serum
339 and 0.2% Tween 20) and incubated with primary antibodies at 4°C overnight, followed by
340 incubation with fluorescently conjugated secondary antibodies for 1 hour at room
341 temperature. All the antibodies were diluted in blocking buffer. Slides were mounted with
342 Vectashield mounting medium containing DAPI for nuclear labelling (Vector Laboratories)
343 and were visualized using an Axio Imager 2 (Zeiss). The list of antibodies for
344 immunofluorescence and RNAscope probes used in this study is presented in the table
345 below.
346 smFISH experiments were conducted as follow. Briefly, to prepare tissue sections
347 for smFISH, infected animals and naïve controls were anesthetized with isoflurane,
348 decapitated and brains were dissected out into ice-cold 1X HBSS. Coronal brain sections
349 were prepared as described above and embedded in paraffin. Cryopreserved coronal brain
350 sections (5 µm) were prepared placed on a SuperFrost Plus microscope slides. Sections
351 were fixed with 4% paraformaldehyde (PFA) at 4 °C for 15 min, and then dehydrated in 50,
352 70 and 100% ethanol. RNAscope 2.5 Assay (Advanced Cell Diagnostics) was used for all
353 smFISH experiments according to the manufacturer's protocols. All RNAscope smFISH
354 probes were designed and validated by Advanced Cell Diagnostics. For image acquisition,
355 16-bit laser scanning confocal images were acquired with a 63x/1.4 plan-apochromat
356 objective using an LSM 710 confocal microscope fitted with a 32-channel spectral detector
357 (Carl Zeiss). Lasers of 405nm, 488nm and 633 nm excited all fluorophores simultaneously
358 with corresponding beam splitters of 405nm and 488/561/633nm in the light path. 9.7nm
359 binned images with a pixel size of 0.07um x 0.07um were captured using the 32-channel
360 spectral array in Lambda mode. Single fluorophore reference images were acquired for
361 each fluorophore and the reference spectra were employed to unmix the multiplex images
362 using the Zeiss online fingerprinting mode. smFISH images were acquired with minor
363 contrast adjustments as needed, and converted to grayscale, to maintain image
364 consistency. The resulting images were processed and analysed using QuPath (Bankhead
365 et al., 2017), and the values plotted using Prism v8.0. The *in situ* hybridisation images were
366 acquired from the publicly available resource the Allen Mouse Brain Atlas
367 (www.mouse.brain-map.org/) and used in Figure S3B.
368
369

List of RNAscope probes used for smFISH			
Supplier	**Cat. Number**	**Sequence**	**Channel**
***Trypanosoma brucei* probes**			
Biotechne	1103198-C1	Tbr-Gapdh	Channel 1
Biotechne	1103208-C2	Tbr-Pyk1	Channel 2
Biotechne	1103218-C3	Tbr-Pad2	Channel 3
Biotechne	1103221-C4	Tbr-Ep1	Channel 4
***Mus musculus* probes**			
Biotechne	460181	Mm-Cd79a	Channel 1
Biotechne	314221-C2	Mm-Cx3cr1	Channel 2
Biotechne	317261-C3	Mm-IL10	Channel 3
Biotechne	517731-C4	Mm-Il10ra	Channel 4
Biotechne	414891-C3	Mm-Tnfsf13b	Channel 3
Biotechne	414871-C4	Mm-Tnfrsf17	Channel 4

370

List of antibodies used for immunofluorescence				
Supplier	**Cat. Number**	**Target**	**Clone**	**Dilution**
Cell Signalling	43279S	Arginase 1- Alexa fluor 647	D4E3M	1:100
Miltenyi	130-114-651	RE-Affinity CD68-PE		1:50
Santa Cruz	sc-33673	GFAP-Alexa Fluor 488	2E1	1:100

371

372 **Flow cytometry analysis and *ex vivo* stimulation of brain-dwelling B cells.** To
373 discriminate circulating versus brain-resident immune cells, we performed intravascular
374 staining of peripheral $CD45^+$ immune cells as previously reported (Anderson et al., 2014).
375 Briefly, a total of 2 μg of anti-CD45-PE antibody (in 100 μl of 1X PBS) was injected
376 intravenously 3 minutes prior culling. Mice were euthanised as described above and
377 transcardially perfused with ice-cold 0.025% (wt/vol) EDTA in 1X PBS. Whole brain samples
378 were collected and placed on ice-cold 1X HBSS (Invitrogen) and processed as recently
379 described (Guldner et al., 2021). Whole brain specimens were minced and digested using
380 the Adult Brain dissociation kit (Miltenyi) for 30 min at 37 °C, following manufacturer's
381 recommendations. The digested tissue was gently pressed through 70 µm nylon mesh cell
382 strainers to obtain a single cell suspension. The cell suspension was cleaned up and
383 separated from myelin debris using a Percoll gradient, as previously reported (Guldner et
384 al., 2021). The resulting fraction was then gently harvested and used as input for glia
385 profiling or for B cell purification using the B cell isolation kit II (negative selection approach)
386 using MACS sorting (Miltenyi). Cells from spleens were used as positive controls. The

387 resulting cell fraction was diluted to a final density of ~1x10^6 cells/ml. The resulting
388 suspension enriched in B cells were seeded on a 96 well plate and stimulated with 1X cell
389 Stimulation cocktail containing phorbol 12-myristate 13-acetate (PMA), Ionomycin, and
390 Brefeldin A (eBioSciences™) for 5 hours at 37°C and 5% CO_2, as previously reported
391 (Radomir et al., 2021). Upon stimulation, the resulting supernatant was harvested and used
392 to quantify IL-10 by ELISA (Biolegend), or to test its capacity to block BV2 polarisation in
393 the presence of *E. coli* LPS. As control, anti-mouse IL-10 antibody (IgG2b, clone JES5-
394 16E3. Biolegend) was applied to the B cell-derived supernatant for 30 min at room
395 temperature to sequester and block IL-10 signalling *in vitro*.
396 For flow cytometry analysis, single cell suspensions were resuspended in ice-cold FACS
397 buffer (2 mM EDTA, 5 U/ml DNAse I, 25 mM HEPES and 2.5% Foetal calf serum (FCS) in
398 1× PBS) and stained for extracellular markers at 1:400 dilution. The list of flow cytometry
399 antibodies used in this study were obtained from Biolegend and are presented in the table
400 below. Samples were run on a flow cytometer LSRFortessa (BD Biosciences) and analysed
401 using FlowJo software version 10 (Treestar). For intracellular staining, single-cell isolates
402 from brain or draining lymph nodes were stimulated as above in Iscove's modified
403 Dulbecco's media (supplemented with 1× non-essential amino acids, 50 U/ml penicillin,
404 50 µg/ml streptomycin, 50 µM β-mercaptoethanol, 1 mM sodium pyruvate and 10% FBS;
405 Gibco). Cells were then permeabilized with a Foxp3/Transcription Factor Staining Buffer Set
406 (eBioscience) and stained for 30 min at 4 °C. All antibodies used were diluted at 1:250.

List of antibodies used for flow cytometry				
Supplier	**Cat. Number**	**Target**	**Clone**	**Dilution**
Thermo	65-0865-14	Fixable viability dye eFluor 780	-	1:1,000
Biolegend	147712	CD45 PE	I3/2.3	2 µg/100 µl i.v.
Biolegend	103133	CD45 Brilliant Violet 421	30-F11	1:400
Biolegend	115555	CD19 Brilliant Violet 711	6D5	1:400
Biolegend	103225	B220 Alexa Fluor 488	RA3-6B2	1:400
Biolegend	142527	CD138 PE-Dazzle 594	281-2	1:400
Biolegend	101219	CD11b Alexa Fluor 488	M1/70	1:400
Biolegend	366507	BAFF APC	1D6	1:400
Biolegend	141727	CD206 Brilliant Violet 711	C068C2	1:400
Miltenyi	130-119-982	O4 APC	REA576	1:800
Miltenyi	130-123-284	ACSA-PE	IH3-18A3	1:800

407
408

409 **Results**

410 **Single cell transcriptomic analysis of the mouse hypothalamus over the course of *T.***
411 ***brucei* infection**

412 To resolve the complexity of the different cell types and transcriptional pathways
413 involved in the CNS response to *T. brucei* infection with as much singularity and spatial
414 resolution as possible, we employed a combined single cell (scRNAseq) and spatial
415 transcriptomic approach (**Figure 1A**), from samples harvested during the onset of the CNS
416 stage (25dpi) and appearance of neurological symptoms (45dpi) (**Figure 1B and C**). The
417 overall inflammation in the brain neuroparenchyma and the meningeal space was confirmed
418 at these time points by histological examination (**Table S1**). To further refine our scRNAseq
419 dataset, we focused on the hypothalamus, given its critical role in controlling circadian
420 behaviour (Rijo-Ferreira et al., 2018; Tesoriero et al., 2018). We obtained a total of 13,195
421 cells with an average of 500 genes/cell and 1,500 transcripts/cell (**Materials and Methods,**
422 **Figure S1**). Overall, we identified 11 clusters spanning 8 cell types, including microglia
423 (clusters 0, 1, 6, and 9), oligodendrocytes/B cells (cluster 7), astrocytes (clusters 2 and 5),
424 T cells (cluster 3), and vascular-associated cells including endothelium (cluster 4), pericytes
425 (cluster 8), and ependymocytes (cluster 10) (**Figure 1D and Table S2B and S2C**). The
426 microglia subclusters were dominated by the expression of putative markers including *C1qa,*
427 *Lyz2, Aif1,* and *Cx3cr1* (Prinz et al., 2021), whereas the astrocyte cluster was characterised
428 by the expression of *bona fide* markers of mature astrocytes, including *Gfap* and *Agt* (**Figure**
429 **1E, Figure S2, and Table S2B**) (Batiuk et al., 2020). The vascular-associated cells were
430 further divided into three *Cldn5*$^{+}$ endothelial cell subclusters, two clusters representing
431 *Pdgfrb*$^{+}$ pericytes/tanycytes, one cluster representing *Acta2*$^{+}$ pericytes, and one *Ccdc153*$^{+}$
432 ependymocyte cluster (**Figure 1E, Figure S3, and S2E Table**). These data are in
433 agreement with the diversity of the glial cell types previously reported in healthy mouse
434 hypothalamus (Chen et al., 2017; Mickelsen et al., 2019).

435 Disease state analysis revealed differential distribution of cells within the microglia,
436 B cell, and T cell clusters in infected samples compared to naïve controls (**Figure 1F**).
437 Furthermore, by computing an *in silico* gene module score to assess the global expression
438 level of inflammatory mediators (e.g., cytokines and chemokines), we identified that
439 responses to chronic *T. brucei* infection (at both 25 and 45dpi) were largely observed in the
440 microglia subclusters (in particular microglia 1 and 2) and, to a lesser extent in endothelial
441 cells, T cells, and adaptive immune cells and were significantly higher than naïve controls
442 (ANOVA, $p < 2.2^{-16}$) (**Figure 1G**). Taken together, our data demonstrate that *T. brucei*

443 infection in the CNS induces an inflammatory response predominantly in microglia, as well
444 as T and B cells, and to a lesser extent in endothelial cells. Notably, we did not detect *T.*
445 *brucei* enough reads in our scRNAseq dataset for downstream analysis, perhaps owing to
446 the low parasite burden in the brain parenchyma; however, we were able to detect them in
447 our spatial transcriptomics dataset (see below).

448 **Spatial transcriptomics reveals *both T. brucei* long slender and stumpy forms**
449 **predominantly in the circumventricular organs**

450 When analysing our spatial transcriptomics datasets, we noted the expression of
451 multiple *T. brucei*-specific genes in infected samples, especially at 45dpi (**Figure 2A and**
452 **S3B Table**). The majority of the *T. brucei*-specific genes were distributed in discrete
453 locations in the mouse forebrain. For example, *Tb927.6.4280* (*GAPDH*), typically associated
454 with slender forms (Briggs et al., 2021; Creek et al., 2015; Kovářová et al., 2018), was highly
455 expressed in spatial clusters 0, 1, 4, 10, 14, and 17, that define the anatomical regions
456 corresponding to cerebral caudoputamen or corpus striatum, thalamus, hippocampus,
457 cerebral cortex, hypothalamus, and the circumventricular organs (CVOs; including the
458 lateral ventricle and the 3rd ventricle) (**Figure 2A, 2B, and S3B Table**). Similarly,
459 Tb927.7.5940 (*PAD2*) was restricted to cluster 17 (**Figure 2A, 2B, and S3B Table).** The
460 localisation of parasites in these brain regions at 45dpi coincided, at least partly, with an
461 increase in the expression of inflammatory mediators in several brain regions, including
462 around cluster 4 and 17 (both CVOs-related clusters) (**Figure 2C**). The spatial distribution
463 of the different developmental stages of *T. brucei* was further confirmed using smFISH
464 against parasite-specific marker genes associated with slender (*GAPDH* and *PYK1*) or
465 stumpy (*PAD2* and *EP1*) life cycle stages (Briggs et al., 2021; Dean et al., 2009) (**Figure**
466 **2D**) and by independent histological scoring (**Table S3B**). These observations confirm that
467 in addition to passage through the blood-brain barrier, African trypanosomes also exploit
468 the CVOs as points of entry into the CNS (Bentivoglio et al., 2018; Kristensson et al., 2010).

469 To provide insights into the potential diversity of brain-dwelling trypanosomes,
470 including the presence of various developmental stages, we performed gene ontology and
471 pathway analysis on the most abundant *T. brucei* transcripts based on their relative spatial
472 distribution (**Figure 2E and S3C Table**). Overall, we observed an overrepresentation of
473 genes typically associated with metabolically active parasites in the CVOs, such as protein
474 translation ($p\ adj = 3.35^{-57}$) and biosynthetic processes ($p\ adj = 1.05^{-24}$), irrespective of their
475 spatial distribution (**Figure 2E and S3C Table**) (Briggs et al., 2021; Creek et al., 2015;
476 Kovářová et al., 2018). Additionally, the transcriptome of the parasites in the CVOs was

477 dominated by genes pathways broadly associated with translation (*p adj* = 9.14^{-22}), control
478 of gene expression (*p adj* = 2.23^{-04}), and biosynthetic processes (*p adj* = 3.46^{-08}), indicating
479 that the CVO-dwelling parasites are metabolically active. Notably, the parasites in the CVOs
480 also expressed genes considered critical regulators of parasite differentiation, such as
481 RBP7A and RBP7B (encoded by *Tb927.10.12090* and *Tb927.10.12100*, respectively),
482 PAD1 (encoded by *Tb927.7.5930*), and PAD2 (encoded by *Tb927.7.5940*) (**S3C Table**)
483 (Dean et al., 2009; Mony et al., 2014; Rojas et al., 2019). Together, these results provide
484 an overview of the spatial distribution of African trypanosomes in the mouse forebrain and
485 support the hypothesis that the majority of brain-dwelling trypanosomes display features of
486 replicative slender forms, protein translation and control of gene expression, together with
487 differentiation commitments in the CVOs.

488 **Infection-associated microglia and border-associated macrophages occupy spatial**
489 **niches in proximity to the ventricular spaces**

490 Having established that microglia display a high inflammatory score upon infection,
491 and *T. brucei* slender and stumpy forms are found in or surrounding CVOs, we next asked
492 whether the spatial distribution of different microglia cell clusters correlates to the distribution
493 of parasites in the forebrain. After subclustering, we identified six discrete myeloid
494 subclusters that displayed a marked differential gene expression signature (**Figure 3A**). For
495 example, cluster 1 and cluster 2 express high levels of putative homeostatic microglia
496 marker genes including *P2ry12, Trem119,* and *Cx3cr1* and may correspond to different
497 homeostatic subsets. Cells in cluster 1 express high levels of *Tgfbr1, Ifngr1*, and *Il6ra*,
498 whereas cluster 2 expresses high levels of *Il10ra* (**Figure 3B and S2F Table**), suggesting
499 a potential divergent response to cytokine signalling (e.g., interferon gamma (IFNγ) in cluster
500 one versus IL-10 in cluster 2). Cluster 3 is characterised by the expression of monocyte-
501 specific lineage markers, including *Cd14*, *Ccrl2, Fcgr2b,* and several MHC-II associated
502 molecules (*H2-Aa1, H2-Ab1*) (**Figure 3B and S2F Table**). Cluster 4 and 5 express high
503 levels of *Aif1*, as well as canonical pro-inflammatory chemokines and mediators of innate
504 immunity (*Ccl5, Mif, Cxcl13*), components of the complement cascade (*C1qa, C1qb*),
505 antigen processing and presentation genes (*H2-Ab1, H2-Eb1*), several interferon-stimulated
506 genes (*Ifitm3, Ifih1*), and markers of disease-associated microglia (*Apoe, Itgax, Trem2,*
507 *Cst7*) (Fitz et al., 2021; Krasemann et al., 2017; Shi and Holtzman, 2018), but decreased
508 expression of microglia homeostatic markers (**Figure 3B and S2F Table**). Lastly, cluster 6
509 expresses putative marker genes associated with border-associated macrophages such as

510 *Lyz2*, *Ms4a7*, *Ms4a6c, Tgfbi, H2-Ab1, and Lyz2* (Van Hove et al., 2019; Jordão et al., 2019),
511 as well as gene sets characteristic of anti-inflammatory responses, such as *Chil3*, *Arg1*, and
512 *Vegfa* (**Figure 3B and S2F Table**), indicative of an anti-inflammatory phenotype. Based on
513 these results we catalogued clusters 1 to 6 as follow: *Cx3cr1*$^+$ 1 (29.5%), *Cx3cr1*$^+$ 2, (30.4%),
514 *Cd14*$^+$ Monocytes (27.6%), *Arg1*$^+$ border-associated macrophages (*Arg1*$^+$ BAMs; 12.6%),
515 *Aif1*$^+$ 1 (10.5%), *Aif1*$^+$ 2 (4.85%) (**Figure 3C and D)**. Notably, *Cx3cr1*$^+$ microglia 1 and 2,
516 and *Cd14*$^+$ monocytes accounted for ~75% of all the microglia detected under homeostatic
517 conditions, but *Aif1*$^+$ microglia 1 and 2*,* and *Arg1*$^+$ BAMs subclusters progressively increased
518 in frequency over the course of infection, suggesting an adoption of an infection-associated
519 phenotype (**Figure 3C and 3D**). In the spatial context, we found that the gene expression
520 of *Aif1*, *Adgre1*, specific marker genes for the *Aif1*$^+$ *1* and *Aif1*$^+$ *2* subclusters, were highly
521 expressed around the hippocampus, CVOs, and caudoputamen at 25dpi and 45dpi
522 compared to naïve controls (**Figure 3F**). Similarly, *Arg1* and *Chil3,* putative marker genes
523 for *Arg1*$^+$ BAMs, were predominantly located in the lateral ventricle and the dorsal 3rd
524 ventricle in the infected brain (**Figure 3E**), further corroborated by immunofluorescence
525 analysis on independent brain sections (**Figure 3F**). Together, our combined analyses
526 demonstrate that infection-associated myeloid subsets (*Aif1*$^+$ 1, *Aif1*$^+$ 2, and *Arg1*$^+$ BAMs)
527 are detected in regions proximal to the CVOs, coinciding with the spatial distribution of
528 trypanosomes and suggesting a functional compartmentalisation of the myeloid subsets in
529 responses to infection.

530 **Microglial responses to *T. brucei* infection share common transcriptional features**
531 **with neurodegeneration diseases**

532 To gain a more comprehensive understanding of microglia responses to infection at
533 the molecular level, we analysed the differentially expressed genes (DEGs) of microglia
534 subtypes in response to *T. brucei* infection, defined as genes with a Log_2 fold change >0.25
535 or <-0.25 and an adjusted *p* value < 0.05. Most of the upregulated DEGs were detected in
536 the *Cx3cr1*$^+$ 1, *Cx3cr1*$^+$ 2, and *Cd14*$^+$ monocyte subclusters (**Figure 3G**) and were
537 associated with an upregulation of MHC-II-mediated antigen presentation (i*H2-Aa1, H2-*
538 *Ab1*), Neutrophil chemotaxis (*Ccl2, Ccl4)*, adaptive immune responses (*Cd274, Mif,*
539 *Tnfsf13b*), and responses to IFNγ (*Ifitm3, Aif1*) (**Figure 3H top and S2G Table**). As the
540 infection progresses, we noted an enrichment for gene pathways associated with
541 neurodegenerative disorders, including Amyotrophic lateral sclerosis, Huntington disease,
542 Parkinson disease, and Alzheimer's disease, including *Apoe, Trem2, Psen2*, and *Cd22*

543 (**Figure 3H bottom and S2G Table)**. These cells also downregulate homeostatic processes
544 associated with organ development (*Tgfbr1, Mertk, Fos*), neurone homeostasis (*Cx3cr1,*
545 *Itgam*), and responses to cAMP (*Fosb, Junb*) (**Figure 3H, S2G and S2H Table**). Overall,
546 our data demonstrates a dynamic response of the microglia during *T. brucei* infection; during
547 the onset of the CNS stage (25dpi), homeostatic *Cx3cr1*$^{+}$ microglia upregulate
548 transcriptional programmes associated with antigen processing and presentation and
549 development of adaptive immune responses, whilst downregulating genes associated with
550 homeostasis. As the infection progresses (45dpi), the microglia signatures share many
551 commonalities to those identified in neurodegenerative disorders (e.g., *Apoe, Trem2, Cd22*)
552 (Fitz et al., 2021; Krasemann et al., 2017; Pluvinage et al., 2019; Shi and Holtzman, 2018),
553 coinciding with the development of clinical symptoms in these animals. These data suggest
554 a common transcriptional response to inflammatory processes in the CNS. Other myeloid
555 cell types such as *Cd14*$^{+}$ monocytes and *Arg1*$^{+}$ BAMs constitute additional responders to
556 the infection, albeit with opposing effects; *Cd14*$^{+}$ monocytes and *Arg1*$^{+}$ BAMs display pro-
557 and anti-inflammatory phenotypes, respectively.

558 **Chronic *T. brucei* infection recruits follicular-like regulatory *Cd4*$^{+}$ T cells and**
559 **cytotoxic *Cd8*$^{+}$ T cells into the CNS**

560 We next sought to characterise the population of adaptive immune cells identified in
561 our dataset. We identified three T cell subclusters based on the expression of putative T cell
562 marker genes such as *Trac* and *Cd3g* (**Figure 4A to 4C, and S2I Table).** Cluster 0 (44%)
563 was discarded owing to the lack of identifiable marker genes. Cluster 1 (18%) and 2 (18.5%)
564 express marker genes associated with cytotoxic T cells such as *Cd8a* and *Gzmb* (**Figure**
565 **4A to 4C, and S2I Table**). Cells within cluster 2 also express high levels of genes associated
566 with cytotoxic T cell activation and effector function (*Ccl5, Klrd1*), a gamma TCR receptor
567 subunit (*Trgv2*), interferon-stimulated genes (*Ifitm1*), and high levels of *Cd52* which is
568 involved in T cell effector function (**S2I Table**) (von Kutzleben et al., 2017). This suggests
569 that cells in cluster 2 potentially represent a specialised cytotoxic T cell subset. Lastly, in
570 addition to *Cd4*, cells in cluster 3 (18.5%) express high levels of genes associated with
571 regulatory CD4^{+} T cells including surface markers (*Cd5, Ctla4, Icos, Cd274*), transcription
572 factors (*Mxd1, Izkf2*), and effector molecules (*Il10, Areg, Il21*) (**Figure 4A to 4C, and S2I**
573 **Table**). Notably, these regulatory *Cd4*$^{+}$ T cells also express high levels of marker genes
574 typically associated with follicular helper T cells such as *Maf* and *Slamf5* (**Figure 4A to 4C,**
575 **and S2I Table**) (Bauquet et al., 2009; Cannons et al., 2010; Nurieva and Chung, 2010).
576 These follicular-like regulatory CD4^{+} T cell subsets have been postulated as critical

577 regulators of adaptive responses in lymphoid organs (Hao et al., 2021a; Miles and Connick,
578 2018; Vaeth et al., 2019, 2019; Wollenberg et al., 2011), but so far have not been reported
579 in the brain during infections. These populations seemed dynamic over the course of
580 infection, with chronic stages associated with a two-fold increase in the abundance of *Cd4*$^+$
581 T cells compared to other subclusters (8.2%, 19.3%, and 20.85% in naïve, 25dpi, and 45dpi,
582 respectively) (**Figure 4B and 4D**), consistent with previous reports (Laperchia et al., 2016;
583 Lyck et al., 2003). Of note, the subcluster identified as cluster 2 *Cd8*$^+$ T cells (*Cd8*$^+$ 2 T cells)
584 was only detected in infected samples but not in naïve controls (23% and 20% at 25 and
585 45dpi, respectively) (**Figure 4B**), indicating a disease-associated T cell subset in the brain.
586 When compared across the brain in the spatial transcriptomics data set, the *Cd4*$^+$ T cell
587 subcluster was mostly detected in the lateral ventricle, external capsule, and the
588 caudoputamen in both naïve and infected samples, whereas the *Cd8*$^+$ T cell subsets
589 showed a more widespread distribution in the brain parenchyma (**Figure 4E**).
590 Cell-cell interaction analysis using NicheNet (Browaeys et al., 2020) revealed a
591 network of molecular communication between T cells, stromal cells, and the vasculature, in
592 infected samples compared to naïve controls (**Figure 4F and 4G**). For instance,
593 ependymocytes and endothelia cells express high levels of *Cxcl10* and *Cxcl12*, respectively,
594 which are critical mediators of lymphocytic recruitment into the brain parenchyma during
595 neuroinflammation (Christensen et al., 2006; Fife et al., 2001; Klein et al., 2005). Microglia
596 also express additional subsets of chemokines (*Ccl2, Ccl3, Ccl4*) with no overlap to those
597 detected in vascular-associated cells (**Figure 4F and 4G**), potentially indicating non-
598 redundant mechanisms of T cell recruitment into the brain parenchyma during infection.
599 Furthermore, the endothelial cells and microglia expressed high levels of cell adhesion
600 markers including *Icam1, Icam2*, and *Pecam1* (**Figure 4F and 4G**), which mediate immune
601 cell transendothelial and extravascular tissue migration (Abadier et al., 2015; Dias et al.,
602 2021; Lyck et al., 2003). We also detected additional mediators of T cell activation, including
603 endothelial cell-derived *Il15* and astrocyte-derived *Il18*, which are involved in T cell
604 activation and enhancement of IFNγ production (Alves et al., 2003; Pien et al., 2000;
605 Sareneva et al., 1998; Strengell et al., 2003; Takeda et al., 1998) (**Figure 4F and 4G**).
606 Together, our data provide an overview of the T cell diversity in the CNS during chronic *T.*
607 *brucei* infection, including regulatory *Cd4*$^+$ T cells that accumulate in the brain over the
608 course of *T. brucei* infection. Moreover, ligand-receptor mediated cell-cell communication
609 suggests that microglia, ependymocytes, endothelial cells, and astrocytes are involved in

610 the recruitment and activation of T cells into the brain during chronic *T. brucei,* albeit through
611 divergent signalling molecules.

612 ***Cd138*$^{+}$ plasma cells are detected in the mouse brain during chronic *T. brucei***
613 **infection**

614 Next, we characterised the cells contributing to the genes expressed in cluster 7
615 (**Figure 1D and S2J Table**). This appeared to represent a heterogeneous grouping of cells
616 expressing high levels of oligodendrocyte markers (*Olig1*, *Sox10*, and *S100b*) and *bona fide*
617 B cell markers (*Cd79a*, *Cd79b*, *Ighm*) (**Figure 1D and S2J Table**). Dimensional reduction
618 analysis after subsetting cluster 7 led us to identify five clusters identified as follow: clusters
619 1 (34.7%) and 2 (11.41%) expressed high levels of *Olig1* and *Pdgfra* and corresponded to
620 oligodendrocytes, cluster 3 (8.48%) corresponds to *Epcam*$^{+}$ neuroepithelium, and cluster 4
621 (6.02%) composed of *Map2*$^{+}$ neurons (**Figure 5A and S2J Table**). Lastly, in addition to
622 *Cd79a* and *Cd79b* (which encode for the B cell receptor), cluster 0 (39.3%) was also
623 characterised by high expression levels of putative markers associated with plasma cells,
624 including surface markers (*Sdc1 or Cd138, Slamf7*) and plasma cell-specific transcription
625 factors (*Prdm1, Xbp1, Irf4*) (**Figure 5A, 5B, and S2J Table)**. These cells also express genes
626 associated with regulatory function, including *Il10* and *Cd274* (**Figure 5A, 5B, and S2J**
627 **Table**), and was thus labelled as *Cd138*$^{+}$ plasma cells. Furthermore, the *Cd138*$^{+}$ plasma
628 cells were detected at low levels in naïve controls (~8% of the cells in this cluster) but
629 increased over the course of infection at 25dpi (61.6%) and 45dpi (88%) (**Figure 5C and**
630 **5D**). The enrichment of *Cd138*$^{+}$ plasma cells during chronic infections was further confirmed
631 by flow cytometry on independent *in vivo* experiments, mirroring the proportions detected
632 by scRNAseq (**Figure 5E and 5F**). Notably, *Cd138*$^{+}$ plasma occupied discrete niches in the
633 naïve brain around the CVOs (dorsal 3rd ventricle) and subthalamic regions (**Figure 5G**),
634 but were preferentially detected in the external capsule, corpus callosum, and lateral
635 ventricle at 25dpi, or in the leptomeninges, cingulate cortex, lateral ventricle, and dorsal 3rd
636 ventricle at 45dpi (**Figure 5G**). Taken together with the flow cytometry findings, these data
637 suggest a potential expansion of this population in the CVOs and proximal regions.
638 Furthermore, the predicted expression of *Il10*, an anti-inflammatory cytokine shown to be
639 expressed in B cells with a regulatory phenotype (Brioschi et al., 2021; Radomir et al., 2021;
640 Rosser and Mauri, 2015), was tested and confirmed by ELISA of *ex vivo* stimulation brain-
641 dwelling B cells from infected mice (**Figure 5H**), corroborating the *in silico* data and
642 indicating a regulatory phenotype. Together, these data show the presence of *Cd138*$^{+}$

643 plasma cells with a regulatory phenotype in the CVOs and leptomeninges in the murine
644 brain during chronic *T. brucei* infection.

645 ***Cd138*$^+$ plasma cell supernatant suppresses microglia polarisation towards an**
646 **inflammatory phenotype**

647 Our scRNAseq data indicats that microglia in the forebrain of *T. brucei*-infected mice
648 express both *Il10ra* and *Il10rb* (which together form the functional IL-10 receptor (Burmeister
649 and Marriott, 2018; Holly A. Swartz, Jessica C. Levenson, 2012; Lobo-Silva et al., 2016)
650 (**Figure 5I**), and that brain-dwelling *Cd138*$^+$ plasma cells produce IL-10 when stimulated *ex*
651 *vivo* (**Figure 5H**). Thus, we hypothesised that plasma cell-derived IL-10 may play a role in
652 modulating pro-inflammatory responses in microglia. *In silico* spatial ligand-receptor
653 interaction analysis around the CVOs identified several significant ligand-receptor
654 interactions upregulated during infection, including *Clec1b-Klrb1c*, involved in regulating NK
655 cell-mediated cytolytic activity (Hao et al., 2006), and *Lpl-Lrp2*, which are involved in ApoE-
656 mediated cholesterol intake in neurons (Spuch et al., 2012) (**Figure S5)**. Additionally, we
657 also identified a robust co-expression of *Il10* and *Il10ra* in the CVOs and leptomeninges
658 (**Figure 5J and Figure S5**), coinciding with the predicted localisation of *Cd138*$^+$ plasma
659 cells at 45dpi, which was independently validated using single molecule fluorescence in situ
660 hybridisation (smFISH) (**Figure 5K**). This confirmed that expression of *Il10* in brain dwelling
661 *Cd138*$^+$ plasma cells and *Il10ra* in homeostatic *Cx3cr1*$^+$ microglia. Next, we hypothesised
662 that the supernatant from stimulated *Cd138*$^+$ plasma cells might also block microglia
663 polarisation towards a pro-inflammatory state. As expected, BV2 microglia-like cells
664 exposed to *E. coli* LPS for 24h expressed high levels of the pro-inflammatory cytokines *Il1*β
665 and *Tnf*α (**Figure 5L**), which was abrogated when BV2 cells were exposed to supernatant
666 from *Cd138*$^+$ plasma cells (**Figure 5L**). Moreover, pre-treatment of the *Cd138*$^+$ plasma cells
667 supernatant with a blocking antibody against IL-10 restores the expression of *Il1*β and *Tnf*α
668 in BV2 microglia, strongly indicating that IL-10 is a key plasma cell-derived anti-inflammatory
669 modulator. Taken together, these data suggest a functional interaction between *Cd138*$^+$
670 plasma cells and microglia mediated, mediated at least partially, by IL-10 signalling.

671 ***Cx3cr1*+ microglia express the B cell pro-survival factor B cell activation factor**
672 **(BAFF) signalling**

673 Having established that microglia, T cells and plasma cells are associated with
674 chronic *T. brucei* infection, we next decided to evaluate relevant cell-cell interactions based
675 on the expression level of canonical ligand-receptor pairs. Of these, we observed a network

676 of complex molecular communication between plasma cells and microglia. A group of
677 ligands were redundantly detected in microglia from *Cx3cr1*$^{+}$ 1, *Cx3cr1*$^{+}$ 2, and *Arg1*$^{+}$ BAMs
678 (*Vcam1, Spp1*, and *Agt*) (**Figure 6A**), whereas a second subset of ligands displayed a more
679 cell-restricted expression profile. For example, the pro-survival factor *Tnfsf13b* (encoding
680 for the B cell survival factor, BAFF) was abundantly expressed upregulated by homeostatic
681 *Cx3cr1*$^{+}$ microglia upon infection, whereas the expression of its cognate receptor *Tnfrsf17*
682 (or B cell maturation antigen, BCMA) was highly expressed in *Cd138*$^{+}$ plasma cells from
683 infected animals (**Figure 6B and 6C**). Furthermore, the expression of *Tnfsf13b* was higher
684 in microglia from infected mice (**Figure 6D**), suggesting that this B cell pro-survival factor is
685 induced upon infection. Spatial ligand-receptor interaction analysis based on co-expression
686 revealed that the co-expression of both the gene for the pro-survival factor, *Tnfsf13b* and
687 the gene for its receptor, *Tnfrsf17,* was restricted to the CVOs and leptomeninges (**Figure**
688 **6E and Figure S5**), as identified for the *Il10-Il10ra* ligand-receptor pair. The expression
689 pattern for these two genes was independently confirmed by smFISH analysis and showed
690 that plasma cells expressing *Tnfrsf17* were in close proximity to microglia expressing
691 *Tnfsf13b*, particularly in the vicinity of the lateral ventricle in the brains of *T. brucei*-infected
692 mice (**Figure 6F and Figure S5**). The expression of BAFF in microglia upon infection was
693 further analysed by flow cytometry experiments (**Figure 6G**), corroborating the *in silico*
694 predictions. Together, our data suggest that crosstalk between microglia and *Cd138*$^{+}$
695 plasma cells; In this context, *Cx3cr1*$^{+}$ microglia promote *Cd138*$^{+}$ plasma cell survival *via*
696 BAFF, and in turn *Cd138*$^{+}$ plasma produce IL-10 to dampen down inflammatory responses
697 in microglia during *T. brucei* infection.
698
699
700
701
702
703
704
705
706
707
708

709 **Discussion**

710 To address fundamental questions regarding the innate and adaptive immune
711 responses of the CNS to unresolved, chronic *T. brucei* infection, this study had three main
712 goals: *i*) to characterise the temporal transcriptional responses of glial and recruited immune
713 cells to the CNS using single cell transcriptomics, *ii*) to understand the spatial distribution of
714 candidate cell types from the scRNAseq dataset using 10X Visium spatial transcriptomics,
715 and *iii*) to model cell-cell interactions taking place in the CNS during chronic infections based
716 on putative ligand-receptor interactions at both single cell and spatial level. Our combined
717 atlas provides novel and important insights for future analyses of the innate and adaptive
718 immune response to chronic CNS infection by *T. brucei*.

719 Our data describe critical and previously unappreciated cell types and cell-cell
720 interactions associated with chronic CNS infections. We demonstrate that microglia drive
721 inflammatory and anti-parasitic responses in the CNS, and also provide insights into the
722 transcriptional features border associated macrophages (BAMs). These responses are
723 heterogeneous, with microglia and *Cd14*$^{+}$ monocytes displaying strong pro-inflammatory
724 signatures. Their transcriptional programme is consistent with pro-inflammatory responses
725 expected to be triggered in response to pathogenic challenges during the onset, including
726 the production of cytokines (i.e., *Il1b, Tnf*), chemokines (i.e., *Ccl5, Cxcl10*), and an
727 upregulation of molecules associated with antigen processing and presentation. Based on
728 the differential gene expression analysis over the course of infection, we propose a model
729 in which homeostatic *Cx3cr1*$^{+}$ microglia undergo extensive transcriptional remodelling
730 during infection, leading to the acquisition of an infection associated phenotype, which
731 coincides with the onset of clinical symptoms. This includes the upregulation of gene
732 programmes involved in other neurodegenerative disorders, such as *Apoe, Trem2,* and
733 *Cd22* at the point of infection in which clinical symptoms are detected (Fitz et al., 2021;
734 Krasemann et al., 2017; Pluvinage et al., 2019; Shi and Holtzman, 2018). The transcriptional
735 signatures identified in the IAMs state are reminiscent of those previously reported in
736 neurodegenerative disorders, thus it is tempting to speculate that this represents a core
737 "pathological" transcriptional module that is triggered in microglia in response to insults,
738 irrespective of the nature of such insults (e.g., parasites versus protein aggregates). These
739 similarities provide new insights into the mechanisms behind chronic brain inflammation.

740 Additionally, our datasets suggest that *Arg1*$^{+}$ BAMs acquire an anti-inflammatory
741 state in the chronically infected brain, which might counterbalance the inflammatory
742 responses of infection-associated microglia (IAM). This is consistent with the responses

743 observed in other organs in which macrophages with an anti-inflammatory phenotype act to
744 limit inflammatory damage by promoting tissue repair (Mosser et al., 2021; Nobs and Kopf,
745 2021; Watanabe et al., 2019; Wynn and Vannella, 2016). To our knowledge, this is the first
746 report describing the responses of the BAMs to infection by protozoan pathogens. Given
747 their seemingly important role in promoting anti-inflammatory responses, further work is
748 required to explore whether these BAMs consists of ependymal (epiplexus or
749 supraependymal macrophages) or stromal choroid plexus macrophages, as recently
750 discussed (Munro et al., 2022).

751 This study also improves our understanding of the components of the adaptive
752 immune response that are recruited into the hypothalamic and brain parenchyma during
753 chronic infection. These include T cells, consistent with previous findings that these cells
754 have a prominent role in modulating CNS responses to *T. brucei* infection (Laperchia et al.,
755 2016; Masocha et al., 2004; Olivera et al., 2021). In addition to conventional cytotoxic *Cd8*$^+$
756 T cells, we have identified a *Cd4*$^+$ T cell subset that shares many features with T follicular
757 helper cells, including the expression of immunomodulatory genes and effector molecules.
758 We also identified and validated, for the first time, a population of *Cd138*$^+$ plasma cells that
759 display a marked regulatory phenotype, characterised by the expression of *Il10, Lgals1*, and
760 *Cd274*. These plasma cells are exclusively detected in chronic infections but not in healthy
761 controls or during the onset of the CNS stage, suggesting a positive correlation between
762 CNS invasion and plasma cell recruitment. Using an *in vitro* approach, we also show that
763 these cells dampen pro-inflammatory responses in microglia mediated by IL-10 signalling,
764 consistent with previous studies (Laffer et al., 2019; Shemer et al., 2020; Sun et al., 2019),
765 although additional factors (e.g., *Lgals1*) might also play a role in this process. *In silico*
766 predictions suggest that microglia, in particular homeostatic microglia, are able to promote
767 plasma cell survival *via Tnfsf13*, encoding the B cell survival factor BAFF (Mackay and
768 Browning, 2002; Mackay et al., 2003; Ng et al., 2004; Smulski and Eibel, 2018). We
769 validated this using smFISH, confirming that both *Tnfsf13* and its cognate receptor *Tnfrsf17*
770 (encoding for the B cell maturation antigen, BCMA) are upregulated in microglia and B cells,
771 respectively, upon infection.

772 Based on these results, we propose a two-phase model to explain the behaviour of
773 microglia and adaptive immune cells over the course of CNS infection by *T. brucei*, centrally
774 coordinated at the CVOs. The first phase, or “priming phase” takes place during the onset
775 of the CNS stage and is associated with an upregulation of genes involved in antigen
776 presentation, cell migration and response to chemokine signalling, potentially derived from

777 peripheral and/or systemic signals. The second stage, or the "pathology phase", and is
778 characterised by the upregulation of a core transcriptional programme previously reported
779 in neurodegenerative disorders, including *Apoe and MHC-II* (Bohlen et al., 2019; Grubman
780 et al., 2021; Sala Frigerio et al., 2019; Shi and Holtzman, 2018; Wang, 2021). This coincides
781 with the worsening of the clinical scoring and the appearance of severe neurological
782 symptoms in this model of infection. In this context, the activation of homeostatic microglia
783 leads to the recruitment and survival of plasma cells mediated by BAFF-BCMA signalling.
784 In turn, these regulatory plasma cells alleviate inflammation by dampening microglia
785 activation *via* IL-10 signalling, limiting pathology, providing novel insights into the
786 mechanisms of B cell-microglia interactions in the brain during infection. Our model is in line
787 with previous work demonstrating that systemic IL-10 administration ameliorates
788 neuroinflammation during chronic *T. brucei* infection (Rodgers et al., 2015), thus highlighting
789 a prominent role of IL-10, derived from either *Cd138*$^{+}$ plasma cells or follicular-like *Cd4*$^{+}$ T
790 cells, in limiting brain pathology. Future work is required to understand the origin of the
791 *Cd138*$^{+}$ plasma cells recruited into the brain parenchyma upon CNS colonisation, but the
792 meningeal space and the lymphopoietic niche at the CNS border is a plausible candidate
793 (Brioschi et al., 2021; Wang et al., 2021b). Our results also demonstrate that the CNS
794 invasion by African trypanosomes is orchestrated and fine-tuned by a myriad of cellular
795 interactions between resident stromal cells and recruited peripheral immune cells in and
796 around the CVOs, suggesting a previously unappreciated role for the CVOs in the
797 pathogenicity of Sleeping Sickness. Although the formation of tertiary lymphoid structures
798 in the CNS upon *T. brucei* infection has not been observed before, we speculate that this
799 population of follicular-like T cells, together with stromal cells that might function to support
800 T-B cell interactions (e.g., ependymal cells) might be involved in supporting primary humoral
801 responses. We suggest that the *Cd138*$^{+}$ plasma cells identified in our study facilitate this
802 response, especially around the CVOs. Further work is required to understand how these
803 various signals translate into changes in sleep/wake patterns and circadian behaviour in
804 sleeping sickness.

805 **Limitations of this study**

806 In this paper, we have provided for the first time a detailed, spatially resolved, single
807 cell atlas of the murine CNS in response to chronic infections with African trypanosomes.
808 Although our work represents a valuable gene expression resource of the murine CNS in
809 response to infection, validated by complementary approaches, further work on examining
810 the expression of other key molecular markers may offer additional information in the field.

Similarly, we have also defined several key cell-cell communications taking place in the infected brain using in silico ligand-receptor interaction analysis, but detailed functional experiments are required to validate their role *in vitro* and *in vivo*. For instance, the origin of the brain-resident plasma cells, observed in the dorsal 3rd ventricle under homeostatic conditions, remains to be evaluated. Additionally, the clonality and antibody repertoire of brain-dwelling plasma cells, expanded after the onset of the CNS stage, merits further investigation. From the parasite perspective, although we did not capture enough parasites in our single cell transcriptomics datasets to make statistical inferences, we have resolved the spatial distribution of slender and stumpy developmental stages and have provided insights into the transcriptional signatures of these developmental stages in different parts of the murine forebrain, which has remained elusive. Future sorting strategies to purify tissue-dwelling parasites will be greatly beneficial to overcome these challenges. We envision that integration of our work with future scRNAseq, and spatial transcriptomic datasets will address some of the questions arising from this study.

Funding and acknowledgments.

We thank Julie Galbraith and Pawel Herzyk (Glasgow Polyomics, University of Glasgow) for their support with library preparation and sequencing. Similarly, we would like to thank the technical staff at the University of Glasgow Biological Services for their assistance in maintaining optimal husbandry conditions and comfort for the animals used in this study. We thank Dr. Jean Rodgers for the work conducted under her Home Office Animal License (PPL No. PC8C3B25C). We thank Dr. Sara Macias Ribela and Dr. Virginia Howick for critically reading this manuscript and for providing feedback. The authors would also like to thank the III Flow cytometry facility for their support with flow cytometry analysis. This work was funded by a Sir Henry Wellcome postdoctoral fellowship (221640/Z/20/Z to JFQ). EMB is funded by a Sir Henry Wellcome postdoctoral fellowship (218648/Z/19/Z). AML is a Wellcome Trust Senior Research fellow (209511/Z/17/Z). PC and MCS are supported by a Wellcome Trust Senior Research fellowship (209511/Z/17/Z) awarded to AML. NAM is supported by project Institute Strategic Programme Grant funding from the BBSRC (BBS/E/D/20231762 and BBS/E/D/20002174). TDO is support by the Wellcome Trust grant (104111/Z/14/ZR). The authors declare that the research was conducted in the absence of any commercial or financial relationships that could be construed as a potential conflict of interest.

Contributions

Methodology: JFQ, AML, NAM, LDL. *In vivo* work and sample collection: JFQ, MCS. Bioinformatic data analysis (single cell transcriptomics): JFQ, PC, EMB, TDO. Bioinformatic data analysis (spatial transcriptomics): JFQ. Flow cytometry: JFQ, MCS. Imaging: JFQ, PC, RH, CAB, CL. The single-cell atlas was created by TDO. All authors participated in discussions related to this work. JFQ wrote the manuscript. All authors reviewed and approved the manuscript.

877 **Figure legend**

878 **Figure 1. Diversity of hypothalamic glial cells during chronic *T. brucei* infection.**
879 **A)** Overview of the experimental approach applied in this work. Upon infection, the levels of
880 parasitaemia (in log_{10} scale; **B**) and clinical scoring **(C)** were measured in infected animals.
881 **D)** Combined UMAP plot for 13,195 high-quality cells coloured by cell type across all the
882 biological replicates. **E)** Heatmap representing the expression level of the top 25 marker
883 genes for each of the cell clusters identified in D. **F)** Frequency of the different cell types
884 detected in the murine hypothalamus at the three experimental groups analysed in this
885 study. **G)** Inflammatory gene module score of genes typically associated with inflammation
886 across all the cell types detected in (D), split and colour-coded by time point of infection.
887 Statistical analysis using analysis of variance (ANOVA) for multiple comparison testing (p =
888 2.2^{-16}) is also reported.

889 **Figure 2. Spatially resolved transcriptomics of brain-dwelling *Trypanosoma brucei*.**
890 **A)** Spatial expression of Tb927.6.4280 (*GAPDH*) and Tb927.7.5940 (*PAD2*) and in the
891 spatial transcriptomics from naïve (top row), 25dpi (middle), and 45dpi (bottom) coronal
892 brain datasets. The circumventricular organs (CVOs)-specific marker Transthyretin (*Ttr*) is
893 included for anatomical reference. **B) Top:** spatial feature plot depicting 18 different
894 transcriptional clusters at in the murine forebrain from infected (45dpi) samples. **Bottom:**
895 Violin plot depicting the relative expression of Tb927.6.4280 (*Gapdh*, marker for slender
896 forms) and Tb927.7.5940 (*Pad2*, marker for stumpy forms) in the different spatially resolved
897 transcriptional clusters in the infected murine brain. *Ttr* (mouse-specific gene) is also
898 included to depict that cluster 17 corresponds to CVOs. Additional regions are also
899 indicated, including caudoputamen or corpus striatum (clusters 0 and 8), hippocampus
900 (cluster 4), Amygdala (cluster 10), and CVOs (cluster 17). The full list of *T. brucei* genes
901 detected can be found in **S3B Table**. **C)** Inflammatory gene module score of genes typically
902 associated with inflammation across the different spatially resolved transcriptional clusters
903 at 45dpi. Non-parametric Wilcox test for multiple comparisons was applied and identified
904 significant differences using the normalised gene expression (basemean) as reference.
905 Asterisk denotes significant differences of <0.05. **D)** Representative smFISH probing
906 putative slender markers *(GAPDH* and *PYK1;* middle panel*)* and stumpy marker genes
907 *(PAD2* and *EP1;* right panels*),* around the lateral ventricle (LV) and choroid plexus (ChP) in
908 naïve animals (left panels) and infected brain samples (right panels). Scale bar = 25 μm. **E)**
909 Top 10 GO terms that characterise brain-dwelling African trypanosomes. The GO terms

910 were chosen using significant genes (-0.25 < Log_2 fold change > 0.25; adjusted *p* value <
911 0.05). Ctx, cerebral cortex; CPu, caudoputamen; Hip, Hippocampus; Am, Amygdala; CVOs,
912 circumventricular organs, including the lateral ventricle (LV) and the dorsal 3rd ventricle
913 (d3V); Th, thalamus.

914 **Figure 3. Diversity and spatial distribution microglia, monocytes, and border-**
915 **associated macrophages during chronic *T. brucei* infection.**

916 **A)** UMAP plot depicting the six subclusters identified as microglia, including the total number
917 of cells in this plot. The dotted line represents the clusters preferentially detected in infected
918 samples compared to naïve controls. **B)** Heatmap representing the expression level of
919 putative microglia marker genes for each of the microglia and myeloid subclusters. The cell
920 origin within each cluster (Naïve in teal, infected in orange) is also indicated at the bottom
921 of the heatmap. **C)** As in (A) but depicting the identified different time points. The dotted line
922 represents the clusters preferentially detected in infected samples compared to naïve
923 controls. **D)** Cell type proportion of the various microglia subclusters detected in Figure 1E
924 over the course of infection. **E)** *In silico* projection of top marker genes for the infection-
925 associated clusters, including *Aif1, Adgre1, Arg1*, and *Chil3* from naïve (top), 25dpi (middle),
926 and 45dpi (bottom) coronal mouse brain sections. Specific brain regions are also indicated.
927 **F)** Imaging analysis of *Arg1*$^+$ BAMs in proximity to the lateral ventricle of naïve and infected
928 mice using immunofluorescence staining for the detection of CD68 (pan-microglia marker)
929 and ARG1 (BAM specific marker). DAPI was included as nuclear staining, and GFAP as a
930 marker for astrocyte reactivity. Scale = 25 μm. **G)** Bar plot indicating the total number of
931 differentially regulated genes (DEGs) at 25dpi (left) and 45dpi (right) compared to naïve
932 controls. Upregulated genes are indicated in red, and downregulated genes are indicated
933 in blue. These genes were defined as having a -2 < Log_2 Fold change < 2, and an adjusted
934 *p* value of < 0.05. **I)** KEGG gene pathways overrepresented in cluster 2 at 25 and 45dpi.

935 **Figure 4. Chronic *T. brucei* infection leads to an expansion of resident follicular-like**
936 ***Cd4*$^+$ T cells in the CNS.**

937 **A)** UMAP plot depicting the three main T cell subclusters identified in figure 1, including the
938 total number of cells in this group. **B)** As in (A) but depicting the identified different time
939 points including in this study. **C)** Heatmap representing the expression level of putative
940 microglia marker genes for each T cell subcluster. The cell origin within each cluster (Naïve
941 in teal, infected in orange) is also indicated. **D)** Proportion of the main T cell subclusters
942 identified in Figure 1E over the course of infection with *T. brucei*. **E)** Spatial feature plot

943 depicting the expression of *Cd4* and *Cd8a*, putative marker genes for *Cd4*$^+$ and *Cd8*$^+$ T cells,
944 respectively, from samples harvested from naïve (top) and 25dpi (middle), and 45dpi
945 (bottom) coronal mouse brain sections. **F)** Circos plot representing significant cell-cell
946 interactions mediated by ligand-receptor communication between T cells (CD4$^+$ and CD8$^+$
947 T cells) and microglia (dark blue), astrocytes (dark green), T cells (dark pink), endothelial
948 cells (light blue), and ependymocytes (light pink). Ligand-receptor interactions that were
949 redundantly observed in more than one cell type are shown in light green. **G)** Heatmap
950 representing the most significant ligand-receptor interactions between T cells and stromal
951 cells detected in the scRNAseq datasets. The ligand-receptor interaction probability is
952 scored based on the prior interaction potential scale. Abbreviations: Ctx, cerebral cortex;
953 CPu, caudoputamen; Hip, Hippocampus; Lateral ventricle (LV); Dorsal 3rd ventricle (d3V).

954 **Figure 5. Chronic *T. brucei* infection is associated with the expansion of resident**
955 **regulatory-like *Cd138*$^+$ plasma cells**

956 **A)** UMAP plot depicting the oligodendrocyte/B cell subclusters, including the total number
957 of cells. **B)** Heatmap of the top 50 most abundant genes in the B cell / oligodendrocyte
958 subcluster, including a second heatmap depicting selected marker genes of plasma cell. **C)**
959 As in (A) but depicting the identified different time points. The dotted line represents the
960 clusters preferentially detected in infected samples compared to naïve controls. **D)**
961 Proportion of the main B cells and oligodendrocytes subclusters identified in Figure 1E over
962 the course of infection with *T. brucei*. **E)** Representative quantification of CD138$^+$ (encoded
963 by *Sdc1*) plasma cells and CD19$^+$ B cells during the first peak of infection (7dpi) and after
964 the onset of the CNS stage (30 dpi) using flow cytometry. **F)** Total number of cells detected
965 by flow cytometry (n = 3-4 mice). A p value of < 0.05 is considered significant. **G)** *In silico*
966 prediction of *Cd138*$^+$ plasma cells distribution onto the spatial transcriptomics slides from
967 naïve (left), 25dpi (middle), and 45dpi (right) coronal mouse brain sections. *Sdc1 or Cd138*,
968 which is a plasma cell-specific marker, is used to depict cell distribution. The relative
969 expression level of is colour coded. **H)** IL-10 production by *ex vivo* brain-dwelling B cells
970 measured by ELISA. An adjusted p value of < 0.05 is considered significant. **I)** Dot Plot
971 representing the expression level of *Il10ra* and *Il10rb* as well as *Il10* in the various cell types
972 identified in naïve and infected mouse hypothalami. **J)** Predicted spatial ligand-receptor
973 interaction analysis for *Il10-Il10ra* in the mouse brain at 45dpi. The relative expression level
974 is indicated, and colour coded. **K)** Representative smFISH imaging targeting *Il10 (red),*
975 *Il10ra (orange), Cd79a (green)*, and *Cx3cr1* (purple) around the lateral ventricle in the
976 infected mouse brain, including an inlet section, highlighting the co-expression of the

977 predicted ligand-receptor pairs. Abbreviations: d3V, dorsal 3rd ventricle; Th, Thalamus; Ctx,
978 Cerebral cortex; CPu, Caudoputamen; LV, Lateral ventricle.
979 **Figure 6. Crosstalk between *Cd138*$^+$ plasma cells and *Cx3cr1*$^+$ microglia in the brain**
980 **of chronically infected animals.**
981 **A)** Circos plot of significant ligand-receptor interactions between *Cd138*$^+$ plasma cells and
982 *Cx3cr1*$^+$ 1 microglia (light blue), *Cx3cr1*$^+$ 1 microglia (dark blue), and *Arg1*$^+$ BAMs (purple).
983 Redundant interactions (shared by >1 cell type) are shown in light green. **B)** Heatmap of the
984 most significant ligand-receptor interactions between *Cd138*$^+$ plasma cells and microglia.
985 **C)** Dot Plot representing the expression level of *Tnfsf13b* (BAFF) and its cognate receptor
986 *Tnfrsf17* (BCMA). **D)** Dot Plot representing the expression level of *Tnfsf13b* (BAFF) in the
987 various microglia subsets identified in the mouse hypothalamus during *T. brucei* infection.
988 **E)** Predicted spatial ligand-receptor interaction analysis for *Tnfsf13b-Tnfrsf17* in the mouse
989 brain at 45dpi. The relative expression level is indicated, and colour coded. **F)** Chronic *T.*
990 *brucei* infection induces the expression of *Tnfsf13b* and *Tnrsf17* in *Cx3cr1*$^+$ microglia and B
991 cells, respectively. Representative smFISH probe targeting *Cx3cr1* (purple), *Cd79a* (green),
992 *Tnfsf13b* (red), and *Tnfrsf17* (orange) around the lateral ventricle (LV) in an infected mouse
993 brain coronal section. Scale, 25 μm. **G)** Representative flow cytometry analysis and
994 quantification of BAFF$^+$ microglia in naïve and infected animals (30 dpi) using flow cytometry
995 (n = 3-4 mice). ** $p < 0.005$ is considered significant.
996
997
998
999
1000
1001
1002
1003
1004
1005
1006
1007
1008
1009

1010 **Supplementary figures**

1011 **Figure S1. Quality control of the hypothalamic scRNAseq datasets over the course of**
1012 **infection with *T. brucei*.**

1013 **A)** Representative flow cytometry analysis from naïve (Top panel) and infected (bottom
1014 panel) animals showing the relative proportion of immune cells ($Cd45^{High}$), microglia
1015 ($CD11b^{High}$ $CD45^{low}$), oligodendrocytes ($O4^{+}$), and astrocytes ($ACSA2^{+}$). **B)** Average
1016 number of genes (top) and transcripts (bottom) per cell in the hypothalamic scRNAseq after
1017 filtering low quality cells, split by biological replicate. For normalisation, we accounted for
1018 differential gene and UMI counts using two independent approaches (SCT and STACAS).
1019 Both packages broadly identified the same cell populations. **C)** Gating strategy for the
1020 identification of resident immune cells, related to the quantification of $CD138^{+}$ plasma cells,
1021 as well as the expression of *Tnfsf13b* and *Tnfrsf17* in microglia and B cells, respectively.

1022 **Figure S2. Transcriptional landscape of hypothalamic astrocytes and vasculature**
1023 **during chronic *T. brucei* infection.**

1024 **A)** UMAP plot depicting the various vascular-associated cell types identified in the
1025 hypothalamic scRNAseq dataset. **B)** Spatial feature plot of putative marker genes for the
1026 various vasculature-associated cells in the 10X Visium dataset from naïve (top), 25dpi
1027 (middle), and 45dpi (bottom) coronal mouse brain sections. The relative expression level is
1028 indicated, and colour coded.

1029 **Figure S3. Quality control of 10X Visium datasets from the mouse forebrain over the**
1030 **course of infection with *T. brucei***

1031 **A)** Spatially resolve cluster genes for naïve (left), 25dpi (middle), and 45dpi (right) 10X
1032 Visium spatial transcriptomics. **B)** Spatially resolved expression level of putative marker
1033 genes defining different anatomical brain regions in naïve (top) and 45dpi (bottom) samples.
1034 The transcriptional patters coincide with in situ hybridisation analysis of the following marker
1035 genes from the Allen Mouse brain atlas: *Camk2* (http://mouse.brain-
1036 map.org/experiment/show/79490122), *Hpca* (http://mouse.brain-
1037 map.org/experiment/show/72129291), *Tcf7l2* (http://mouse.brain-
1038 map.org/experiment/show/72339557), *Vipr2* (http://mouse.brain-
1039 map.org/experiment/show/1104), *Adora2a* (http://mouse.brain-
1040 map.org/experiment/show/72109410), *Ttr* (http://mouse.brain-
1041 map.org/experiment/show/68632172) (Daigle et al., 2018; Harris et al., 2019; Lein et al.,
1042 2007; Oh et al., 2014).

1043 **Figure S4. Characterisation of CNS myeloid responses to T. brucei infection.**

1044 **A)** Imaging analysis of *Arg1*$^{+}$ BAMs in coronal brain sections of naïve and 45 day-infected
1045 mice using immunofluorescence staining for the detection of CD68 (pan-microglia marker)
1046 and ARG1 (BAM specific marker). DAPI was included as nuclear staining, and GFAP as a
1047 marker for astrocyte reactivity. An IgG isotype control is also included. Scale bar = 25 μm.
1048 **B)** Examples of downregulated gene pathways overrepresented in *Cx3cr1*$^{+}$ 2 microglia at
1049 25 and 45dpi.

1050 **Figure S5. Ligand-receptor interaction network in the mouse brain at 45 days post-**
1051 **infection.**

1052 **A)** Spatially resolved cluster genes for the 45dpi 10X Visium spatial transcriptomic dataset.
1053 **B)** Uniform Manifold Approximation and Projection (UMAP) plot depicting the predicted
1054 cluster-cluster interactions in the spatial context. Clusters are grouped based on their
1055 predicted ligand-receptor interaction. **C)** Heatmap representing the top 5 most significantly
1056 enriched ligand-receptor pairs in each of the spatially resolved transcriptional units in (A)
1057 and (B), clustered based on their relative expression.

1058 **Figure S6. Microglia – plasma cell communication mediated by *Il10* and *Tnfsf13b*.**

1059 **A)** Chronic *T. brucei* infection induces the expression of *Il10* and *Il10ra* in B cells and
1060 *Cx3cr1*$^{+}$ microglia, respectively. Representative smFISH probe targeting *Cx3cr1* (purple),
1061 *Cd79a* (green), *Il10* (red), and *Il10ra* (orange) around the lateral ventricle (LV) in naïve (left)
1062 and infected (right) mouse brain coronal section. Scale bar, 25 μm. **B) Top panel**: Insets
1063 taken from the infected sample in (A), representing B cells expressing *Il10* (left) and *Cx3cr1*$^{+}$
1064 microglia expressing *Il10ra* (right). **Bottom panel**: Quantification of fluorescence intensity
1065 of the smFISH probes across four biological replicates per group and from >1,000
1066 cells/replicate. Non-parametric *T* test *p* value < 0.01 is considered significant. **C)** Chronic
1067 *T. brucei* infection induces the expression of *Tnfsf13b* and *Tnfrsf17* in *Cx3cr1*$^{+}$ microglia and
1068 plasma cells, respectively. Representative smFISH probe targeting *Cx3cr1* (purple), *Cd79a*
1069 (green), *Tnfsf13b* (red), and *Tnfrsf17* (orange) around the lateral ventricle (LV) in naïve (left)
1070 and infected (right) mouse brain coronal section. Scale bar, 25 μm. **D) Top panel**: Insets
1071 taken from the infected sample in (A), representing plasma cells expressing *Tnfrsf17* (left)
1072 and *Cx3cr1*$^{+}$ microglia expressing *Tnfsf13b* (right). **Bottom panel**: Quantification of
1073 fluorescence intensity of the smFISH probes across four biological replicates per group and
1074 from >1,000 cells/replicate. P value < 0.01 (non-parametric *T* test) is considered significant.
1075 G) Proposed microglia-plasma cell crosstalk mediated by *Il10* and *Tnfsf13b*. In this context,
1076 microglia promote plasma cell maintenance and survival via *Tnfsf13b* (BAFF) signalling,

whereas plasma cells dampen pro-inflammatory responses in microglia via *Il10* signalling. **E)** Proposed model to explain the reciprocal cell-cell communication between plasma cells and homeostatic microglia mediated by IL-10 and BAFF signalling. In this context, plasma cells limit inflammatory processes triggered in homeostatic microglia *via* IL-10 signalling (that undergo transcriptional changes towards an infection-associated phenotype). In turn, microglia promote plasma cell activation and survival *via* BAFF signalling.

1111 **Table legend**

1112 **Table S1. Characterisation of intra- and extra-ventricular trypanosomes in the mouse**
1113 **forebrain.** Histopathology analysis from C57BL/6 female mice infected with *T. brucei brucei*
1114 Antat 1.1E were harvested at 25- and 45- days post-infection (*n* = 3-4 mice/group), fixed in
1115 10% PFA and counterstained with the *T. brucei*-specific antibody TbHSP70. Uninfected
1116 animals (*n* = 3) were included as naïve controls. Clinical scoring on coronal sections were
1117 scored using a double-blinded approach. In addition to relative parasite localisation, H&E
1118 staining was also included to assess meningeal and parenchymal inflammation. The
1119 classification used for the scoring system is included in the table.

1120 **Table S2. Overview of the mouse hypothalamic single cell transcriptomics during**
1121 **chronic *T. brucei* infection. S2A)** Quality control including mean reads per cell and median
1122 genes per cell before and after filtering out low quality cell types. **S2B)** Overview of the major
1123 cell types detected in the single cell dataset at a resolution of 0.4. The total number of cells
1124 per cluster, percentages, and marker genes are also included. **S2C)** Overview of the outputs
1125 generated by scCATCH and SingleR. The predicted cell identity, as well as the prediction
1126 score (where applicable), are included. **S2D)** Marker genes detected with the integration
1127 workflow STACAS for the cells detected in the hypothalamic dataset, and the microglia
1128 subset. **S2E)** Overview of the vascular-associated cells detected in our hypothalamic
1129 dataset at a resolution of 0.3. The marker genes for these clusters, as well as representative
1130 UMAP plots are also included. **S2F)** As in S2E but for the microglia/macrophage subclusters
1131 at a resolution of 0.3**. S2G)** List of differentially expressed genes in all the myeloid subsets
1132 at 25dpi, defined having a $-0.25 < Log_2Fold\ change > 0.25$ and an adjusted *p* value < 0.05.
1133 **S2H)** List of differentially expressed genes in all the myeloid subsets at 45dpi, defined
1134 having a $-0.25 < Log_2Fold\ change > 0.25$ and an adjusted *p* value < 0.05. **S2I)** As in S2E but
1135 for T cells at a resolution of 0.3. **S2J)** Overview of the oligodendrocytes and B cells detected
1136 in our hypothalamic dataset at a resolution of 0.3. The marker genes for these clusters, cell
1137 counts, as well as representative UMAP plots are also included.

1138 **Table S3. Overview of the spatial transcriptomics of the mouse forebrain during**
1139 **chronic *T. brucei* infection. S3A)** Overview of the spatial transcriptomics project, including
1140 total number of reads sequenced per biological replicate, the median number of genes per
1141 spot and the percentage of mappable reads to the mouse (mm10) or *T. brucei* (TREU927)
1142 genomes. **S3B)** Mouse and *T. brucei* marker genes identified in the 10X Visium spatial
1143 transcriptomics datasets. **S3C**) Gene Ontology analysis (Biological processes) generated

using TriTrypDB and default settings. Significantly enriched pathways are defined as having an adjusted p value < 0.05.

1178 **References**

1179 Abadier, M., Haghayegh Jahromi, N., Cardoso Alves, L., Boscacci, R., Vestweber, D.,
1180 Barnum, S., Deutsch, U., Engelhardt, B., and Lyck, R. (2015). Cell surface levels of
1181 endothelial ICAM-1 influence the transcellular or paracellular T-cell diapedesis across the
1182 blood-brain barrier. Eur. J. Immunol. *45*, 1043–1058.
1183 Alves, N.L., Hooibrink, B., Arosa, F.A., and Van Lier, R.A.W. (2003). IL-15 induces
1184 antigen-independent expansion and differentiation of human naive CD8+ T cells in vitro.
1185 Blood *102*, 2541–2546.
1186 Anderson, K.G., Mayer-Barber, K., Sung, H., Beura, L., James, B.R., Taylor, J.J., Qunaj,
1187 L., Griffith, T.S., Vezys, V., Barber, D.L., et al. (2014). Intravascular staining for
1188 discrimination of vascular and tissue leukocytes. Nat. Protoc. *9*, 209–222.
1189 Andreatta, M., and Carmona, S.J. (2021). STACAS: Sub-Type Anchor Correction for
1190 Alignment in Seurat to integrate single-cell RNA-seq data. Bioinformatics *37*, 882–884.
1191 Aran, D., Looney, A.P., Liu, L., Wu, E., Fong, V., Hsu, A., Chak, S., Naikawadi, R.P.,
1192 Wolters, P.J., Abate, A.R., et al. (2019). Reference-based analysis of lung single-cell
1193 sequencing reveals a transitional profibrotic macrophage. Nat. Immunol. *20*, 163–172.
1194 Aslett, M., Aurrecoechea, C., Berriman, M., Brestelli, J., Brunk, B.P., Carrington, M.,
1195 Depledge, D.P., Fischer, S., Gajria, B., Gao, X., et al. (2009). TriTrypDB: A functional
1196 genomic resource for the Trypanosomatidae. Nucleic Acids Res. *38*, 457–462.
1197 Bankhead, P., Loughrey, M.B., Fernández, J.A., Dombrowski, Y., McArt, D.G., Dunne,
1198 P.D., McQuaid, S., Gray, R.T., Murray, L.J., Coleman, H.G., et al. (2017). QuPath: Open
1199 source software for digital pathology image analysis. Sci. Rep. *7*, 1–7.
1200 Barrett, M.P., Chandramohan, D., and Checchi, F. (2008). The Natural Progression of
1201 Gambiense Sleeping Sickness : What Is the Evidence ? PLoS Negl. Trop. Dis. *2*, e303.
1202 Batiuk, M.Y., Martirosyan, A., Wahis, J., de Vin, F., Marneffe, C., Kusserow, C., Koeppen,
1203 J., Viana, J.F., Oliveira, J.F., Voet, T., et al. (2020). Identification of region-specific
1204 astrocyte subtypes at single cell resolution. Nat. Commun. *11*, 1–15.
1205 Bauquet, A.T., Jin, H., Paterson, A.M., Mitsdoerffer, M., Ho, I.C., Sharpe, A.H., and
1206 Kuchroo, V.K. (2009). The costimulatory molecule ICOS regulates the expression of c-Maf
1207 and IL-21 in the development of follicular T helper cells and TH -17 cells. Nat. Immunol.
1208 *10*, 167–175.
1209 Bentivoglio, M., Kristensson, K., and Rottenberg, M.E. (2018). Circumventricular Organs
1210 and Parasite Neurotropism: Neglected Gates to the Brain? Front. Immunol. *9*, 2877.
1211 Bohlen, C.J., Friedman, B.A., Dejanovic, B., and Sheng, M. (2019). Microglia in Brain

1212 Development, Homeostasis, and Neurodegeneration. Annu. Rev. Genet. *53*, 263–288.
1213 Briggs, E.M., Rojas, F., McCulloch, R., Matthews, K.R., and Otto, T.D. (2021). Single-cell
1214 transcriptomic analysis of bloodstream Trypanosoma brucei reconstructs cell cycle
1215 progression and developmental quorum sensing. Nat. Commun. *12*.
1216 Brioschi, S., Wang, W. Le, Peng, V., Wang, M., Shchukina, I., Greenberg, Z.J., Bando,
1217 J.K., Jaeger, N., Czepielewski, R.S., Swain, A., et al. (2021). Heterogeneity of meningeal
1218 B cells reveals a lymphopoietic niche at the CNS borders. Science (80-.). *373*.
1219 Browaeys, R., Saelens, W., and Saeys, Y. (2020). NicheNet: modeling intercellular
1220 communication by linking ligands to target genes. Nat. Methods *17*, 159–162.
1221 Burmeister, A.R., and Marriott, I. (2018). The interleukin-10 family of cytokines and their
1222 role in the CNS. Front. Cell. Neurosci. *12*, 1–13.
1223 Cannons, J.L., Qi, H., Lu, K.T., Dutta, M., Gomez-Rodriguez, J., Cheng, J., Wakeland,
1224 E.K., Germain, R.N., and Schwartzberg, P.L. (2010). Optimal Germinal Center Responses
1225 Require a Multistage T Cell:B Cell Adhesion Process Involving Integrins, SLAM-
1226 Associated Protein, and CD84. Immunity *32*, 253–265.
1227 Carow, B., Hauling, T., Qian, X., Kramnik, I., Nilsson, M., and Rottenberg, M.E. (2019).
1228 Spatial and temporal localization of immune transcripts defines hallmarks and diversity in
1229 the tuberculosis granuloma. Nat. Commun. *10*, 1–15.
1230 Chen, R., Wu, X., Jiang, L., and Zhang, Y. (2017). Single-Cell RNA-Seq Reveals
1231 Hypothalamic Cell Diversity. Cell Rep. *18*, 3227–3241.
1232 Choudhary, S., and Satija, R. (2022). Comparison and evaluation of statistical error
1233 models for scRNA-seq. Genome Biol. *23*, 1–20.
1234 Christensen, J.E., de Lemos, C., Moos, T., Christensen, J.P., and Thomsen, A.R. (2006).
1235 CXCL10 Is the Key Ligand for CXCR3 on CD8 + Effector T Cells Involved in Immune
1236 Surveillance of the Lymphocytic Choriomeningitis Virus-Infected Central Nervous System .
1237 J. Immunol. *176*, 4235–4243.
1238 Creek, D.J., Mazet, M., Achcar, F., Anderson, J., Kim, D.H., Kamour, R., Morand, P.,
1239 Millerioux, Y., Biran, M., Kerkhoven, E.J., et al. (2015). Probing the Metabolic Network in
1240 Bloodstream-Form Trypanosoma brucei Using Untargeted Metabolomics with Stable
1241 Isotope Labelled Glucose. PLoS Pathog. *11*, 1–25.
1242 Daigle, T.L., Madisen, L., Hage, T.A., Valley, M.T., Knoblich, U., Larsen, R.S., Takeno,
1243 M.M., Huang, L., Gu, H., Larsen, R., et al. (2018). A Suite of Transgenic Driver and
1244 Reporter Mouse Lines with Enhanced Brain-Cell-Type Targeting and Functionality. Cell
1245 *174*, 465-480.e22.

1246 Dean, S., Marchetti, R., Kirk, K., and Matthews, K.R. (2009). A surface transporter family
1247 conveys the trypanosome differentiation signal. Nature *459*, 213–217.
1248 Dias, M.C., Quesada, A.O., Soldati, S., Bösch, F., Gruber, I., Hildbrand, T., Sönmez, D.,
1249 Khire, T., Witz, G., McGrath, J.L., et al. (2021). Brain endothelial tricellular junctions as
1250 novel sites for T cell diapedesis across the blood-brain barrier. J. Cell Sci. *134*.
1251 Etet, P.F.S., Palomba, M., Colavito, V., Grassi-Zucconi, G., Bentivoglio, M., and Bertini, G.
1252 (2012). Sleep and rhythm changes at the time of Trypanosoma brucei invasion of the brain
1253 parenchyma in the rat. Chronobiol. Int. *29*, 469–481.
1254 Fèvre, E.M., Wissmann, B. V., Welburn, S.C., and Lutumba, P. (2008). The burden of
1255 human African Trypanosomiasis. PLoS Negl. Trop. Dis. *2*.
1256 Fife, B.T., Kennedy, K.J., Paniagua, M.C., Lukacs, N.W., Kunkel, S.L., Luster, A.D., and
1257 Karpus, W.J. (2001). CXCL10 (IFN-γ-Inducible Protein-10) Control of Encephalitogenic
1258 CD4 + T Cell Accumulation in the Central Nervous System During Experimental
1259 Autoimmune Encephalomyelitis . J. Immunol. *166*, 7617–7624.
1260 Fitz, N.F., Nam, K.N., Wolfe, C.M., Letronne, F., Playso, B.E., Iordanova, B.E., Kozai,
1261 T.D.Y., Biedrzycki, R.J., Kagan, V.E., Tyurina, Y.Y., et al. (2021). Phospholipids of APOE
1262 lipoproteins activate microglia in an isoform-specific manner in preclinical models of
1263 Alzheimer's disease. Nat. Commun. *12*, 1–18.
1264 Grubman, A., Choo, X.Y., Chew, G., Ouyang, J.F., Sun, G., Croft, N.P., Rossello, F.J.,
1265 Simmons, R., Buckberry, S., Landin, D.V., et al. (2021). Transcriptional signature in
1266 microglia associated with Aβ plaque phagocytosis. Nat. Commun. *12*.
1267 Guldner, I.H., Golomb, S.M., Wang, Q., Wang, E., and Zhang, S. (2021). Isolation of
1268 mouse brain-infiltrating leukocytes for single cell profiling of epitopes and transcriptomes.
1269 STAR Protoc. *2*.
1270 Hao, H., Nakayamada, S., and Tanaka, Y. (2021a). Differentiation, functions, and roles of
1271 T follicular regulatory cells in autoimmune diseases. Inflamm. Regen. *41*, 4–11.
1272 Hao, L., Klein, J., and Nei, M. (2006). Heterogeneous but conserved natural killer receptor
1273 gene complexes in four major orders of mammals. Proc. Natl. Acad. Sci. U. S. A. *103*,
1274 3192–3197.
1275 Hao, Y., Hao, S., Andersen-Nissen, E., Mauck, W.M., Zheng, S., Butler, A., Lee, M.J.,
1276 Wilk, A.J., Darby, C., Zager, M., et al. (2021b). Integrated analysis of multimodal single-
1277 cell data. Cell *184*, 3573-3587.e29.
1278 Harris, J.A., Mihalas, S., Hirokawa, K.E., Whitesell, J.D., Choi, H., Bernard, A., Bohn, P.,
1279 Caldejon, S., Casal, L., Cho, A., et al. (2019). Hierarchical organization of cortical and

1280 thalamic connectivity. Nature *575*, 195–202.
1281 Herbert, W.J., and Lumsden, W.H.R. (1976). Trypanosoma brucei: A rapid “matching”
1282 method for estimating the host’s parasitemia. Exp. Parasitol. *40*, 427–431.
1283 Holly A. Swartz, Jessica C. Levenson, and E.F.U. (2012). Interleukin 10 Receptor
1284 Signaling: Master Regulator of Intestinal Mucosal Homeostasis in Mice and Humans.
1285 Physiol. Behav. *43*, 145–153.
1286 Van Hove, H., Martens, L., Scheyltjens, I., De Vlaminck, K., Pombo Antunes, A.R., De
1287 Prijck, S., Vandamme, N., De Schepper, S., Van Isterdael, G., Scott, C.L., et al. (2019). A
1288 single-cell atlas of mouse brain macrophages reveals unique transcriptional identities
1289 shaped by ontogeny and tissue environment. Nat. Neurosci. *22*, 1021–1035.
1290 Jiang, J., Wang, C., Qi, R., Fu, H., and Ma, Q. (2020). scREAD: A Single-Cell RNA-Seq
1291 Database for Alzheimer’s Disease. IScience *23*.
1292 Jordão, M.J.C., Sankowski, R., Brendecke, S.M., Sagar, Locatelli, G., Tai, Y.H., Tay, T.L.,
1293 Schramm, E., Armbruster, S., Hagemeyer, N., et al. (2019). Neuroimmunology: Single-cell
1294 profiling identifies myeloid cell subsets with distinct fates during neuroinflammation.
1295 Science (80-.). *363*.
1296 Klein, R.S., Lin, E., Zhang, B., Luster, A.D., Tollett, J., Samuel, M.A., Engle, M., and
1297 Diamond, M.S. (2005). Neuronal CXCL10 Directs CD8 + T-Cell Recruitment and Control
1298 of West Nile Virus Encephalitis . J. Virol. *79*, 11457–11466.
1299 Kovářová, J., Nagar, R., Faria, J., Ferguson, M.A.J., Barrett, M.P., and Horn, D. (2018).
1300 Gluconeogenesis using glycerol as a substrate in bloodstream-form Trypanosoma brucei.
1301 PLoS Pathog. *14*, 1–22.
1302 Krasemann, S., Madore, C., Cialic, R., Baufeld, C., Calcagno, N., El Fatimy, R., Beckers,
1303 L., O’Loughlin, E., Xu, Y., Fanek, Z., et al. (2017). The TREM2-APOE Pathway Drives the
1304 Transcriptional Phenotype of Dysfunctional Microglia in Neurodegenerative Diseases.
1305 Immunity *47*, 566-581.e9.
1306 Kristensson, K., Nygård, M., Bertini, G., and Bentivoglio, M. (2010). African trypanosome
1307 infections of the nervous system: Parasite entry and effects on sleep and synaptic
1308 functions. Prog. Neurobiol. *91*, 152–171.
1309 von Kutzleben, S., Pryce, G., Giovannoni, G., and Baker, D. (2017). Depletion of CD52-
1310 positive cells inhibits the development of central nervous system autoimmune disease, but
1311 deletes an immunetolerance promoting CD8 t-cell population. Implications for secondary
1312 autoimmunity of alemtuzumab in multiple sclerosis. Immunology *150*, 444–455.
1313 Laffer, B., Bauer, D., Wasmuth, S., Busch, M., Jalilvand, T.V., Thanos, S., Meyer zu

1314 Hörste, G., Loser, K., Langmann, T., Heiligenhaus, A., et al. (2019). Loss of IL-10
1315 Promotes Differentiation of Microglia to a M1 Phenotype. Front. Cell. Neurosci. *13*, 1–12.
1316 Laperchia, C., Palomba, M., Seke Etet, P.F., Rodgers, J., Bradley, B., Montague, P.,
1317 Grassi-Zucconi, G., Kennedy, P.G.E., and Bentivoglio, M. (2016). Trypanosoma brucei
1318 Invasion and T-cell Infiltration of the Brain Parenchyma in Experimental Sleeping
1319 Sickness: Timing and Correlation with Functional Changes. PLoS Negl. Trop. Dis. *10*, 1–
1320 19.
1321 Lein, E.S., Hawrylycz, M.J., Ao, N., Ayres, M., Bensinger, A., Bernard, A., Boe, A.F.,
1322 Boguski, M.S., Brockway, K.S., Byrnes, E.J., et al. (2007). Genome-wide atlas of gene
1323 expression in the adult mouse brain. Nature *445*, 168–176.
1324 Lobo-Silva, D., Carriche, G.M., Castro, A.G., Roque, S., and Saraiva, M. (2016).
1325 Balancing the immune response in the brain: IL-10 and its regulation. J.
1326 Neuroinflammation *13*, 1–10.
1327 Lundkvist, G.B., Kristensson, K., and Bentivoglio, M. (2004). Why trypanosomes cause
1328 sleeping sickness. Physiology *19*, 198–206.
1329 Lyck, R., Reiss, Y., Gerwin, N., Greenwood, J., Adamson, P., and Engelhardt, B. (2003).
1330 T-cell interaction with ICAM-1/ICAM-2 double-deficient brain endothelium in vitro: The
1331 cytoplasmic tail of endothelial ICAM-1 is necessary for transendothelial migration of T
1332 cells. Blood *102*, 3675–3683.
1333 Ma, F., Hughes, T.K., Teles, R.M.B., Andrade, P.R., de Andrade Silva, B.J., Plazyo, O.,
1334 Tsoi, L.C., Do, T., Wadsworth, M.H., Oulee, A., et al. (2021). The cellular architecture of
1335 the antimicrobial response network in human leprosy granulomas. Nat. Immunol. *22*, 839–
1336 850.
1337 Mackay, F., and Browning, J.L. (2002). BAFF: A fundamental survival factor for B cells.
1338 Nat. Rev. Immunol. *2*, 465–475.
1339 Mackay, F., Schneider, P., Rennert, P., and Browning, J. (2003). BAFF and APRIL: A
1340 tutorial on B cell survival. Annu. Rev. Immunol. *21*, 231–264.
1341 Maclean, L., Reiber, H., Kennedy, P.G.E., and Sternberg, J.M. (2012). Stage Progression
1342 and Neurological Symptoms in Trypanosoma brucei rhodesiense Sleeping Sickness : Role
1343 of the CNS Inflammatory Response. PLoS Negl. Trop. Dis. *6*, e1857.
1344 Mantri, A.M., Hinchman, M.M., Mckellar, D.W., Wang, M.F.Z., and Shaun, T. (2021).
1345 Spatiotemporal transcriptomics reveals pathogenesis of viral myocarditis.
1346 Masocha, W., Robertson, B., Rottenberg, M.E., Mhlanga, J., Sorokin, L., and Kristensson,
1347 K. (2004). Cerebral vessel laminins and IFN-γ define Trypanosoma brucei brucei

1348 penetration of the blood-brain barrier. J. Clin. Invest. *114*, 689–694.
1349 Mathys, H., Davila-Velderrain, J., Peng, Z., Gao, F., Mohammadi, S., Young, J.Z., Menon,
1350 M., He, L., Abdurrob, F., Jiang, X., et al. (2019). Single-cell transcriptomic analysis of
1351 Alzheimer's disease. Nature *570*, 332–337.
1352 McCarthy, D.J., Campbell, K.R., Lun, A.T.L., and Wills, Q.F. (2017). Scater: Pre-
1353 processing, quality control, normalization and visualization of single-cell RNA-seq data in
1354 R. Bioinformatics *33*, 1179–1186.
1355 Mickelsen, L.E., Bolisetty, M., Chimileski, B.R., Fujita, A., Beltrami, E.J., Costanzo, J.T.,
1356 Naparstek, J.R., Robson, P., and Jackson, A.C. (2019). Single-cell transcriptomic analysis
1357 of the lateral hypothalamic area reveals molecularly distinct populations of inhibitory and
1358 excitatory neurons. Nat. Neurosci. *22*, 642–656.
1359 Miles, B., and Connick, E. (2018). Control of the germinal center by follicular regulatory t
1360 cells during infection. Front. Immunol. *9*.
1361 Mony, B.M., MacGregor, P., Ivens, A., Rojas, F., Cowton, A., Young, J., Horn, D., and
1362 Matthews, K. (2014). Genome-wide dissection of the quorum sensing signalling pathway
1363 in Trypanosoma brucei. Nature *505*, 681–685.
1364 Mosser, D.M., Hamidzadeh, K., and Goncalves, R. (2021). Macrophages and the
1365 maintenance of homeostasis. Cell. Mol. Immunol. *18*, 579–587.
1366 Munro, D.A.D., Movahedi, K., and Priller, J. (2022). Macrophage compartmentalization in
1367 the brain and cerebrospinal fluid system. Sci. Immunol. *7*, 1–15.
1368 Ng, L.G., Sutherland, A.P.R., Newton, R., Qian, F., Cachero, T.G., Scott, M.L., Thompson,
1369 J.S., Wheway, J., Chtanova, T., Groom, J., et al. (2004). B Cell-Activating Factor
1370 Belonging to the TNF Family (BAFF)-R Is the Principal BAFF Receptor Facilitating BAFF
1371 Costimulation of Circulating T and B Cells. J. Immunol. *173*, 807–817.
1372 Nobs, S.P., and Kopf, M. (2021). Tissue-resident macrophages: guardians of organ
1373 homeostasis. Trends Immunol. *42*, 495–507.
1374 Nurieva, R.I., and Chung, Y. (2010). Understanding the development and function of T
1375 follicular helper cells. Cell. Mol. Immunol. *7*, 190–197.
1376 Oh, S.W., Harris, J.A., Ng, L., Winslow, B., Cain, N., Mihalas, S., Wang, Q., Lau, C., Kuan,
1377 L., Henry, A.M., et al. (2014). A mesoscale connectome of the mouse brain. Nature *508*,
1378 207–214.
1379 Olivera, G.C., Vetter, L., Tesoriero, C., Gallo, F. Del, Hedberg, G., Basile, J., and
1380 Rottenberg, M.E. (2021). Role of T cells during the cerebral infection with trypanosoma
1381 brucei. PLoS Negl. Trop. Dis. *15*, 1–22.

1382 Pien, G.C., Satoskar, A.R., Takeda, K., Akira, S., and Biron, C.A. (2000). Cutting Edge:
1383 Selective IL-18 Requirements for Induction of Compartmental IFN-γ Responses During
1384 Viral Infection. J. Immunol. *165*, 4787–4791.
1385 Pluvinage, J. V., Haney, M.S., Smith, B.A.H., Sun, J., Iram, T., Bonanno, L., Li, L., Lee,
1386 D.P., Morgens, D.W., Yang, A.C., et al. (2019). CD22 blockade restores homeostatic
1387 microglial phagocytosis in ageing brains. Nature *568*, 187–192.
1388 Prinz, M., Masuda, T., Wheeler, M.A., and Quintana, F.J. (2021). Microglia and Central
1389 Nervous System-Associated Macrophages mdash from Origin to Disease Modulation.
1390 Annu. Rev. Immunol. *39*, 251–277.
1391 Radomir, L., Kramer, M.P., Perpinial, M., Schottlender, N., Rabani, S., David, K., Wiener,
1392 A., Lewinsky, H., Becker-Herman, S., Aharoni, R., et al. (2021). The survival and function
1393 of IL-10-producing regulatory B cells are negatively controlled by SLAMF5. Nat. Commun.
1394 *12*, 1–14.
1395 Raredon, M.S.B., Yang, J., Kothapalli, N., Kaminski, N., Niklason, L.E., and Kluger, Y.
1396 (2022). Comprehensive visualization of cell-cell interactions in single-cell and spatial
1397 transcriptomics with NICHES. BioRxiv 1–19.
1398 Le Ray, D., Barry, J.D., Easton, C., and Vickerman, K. (1977). First tsetse fly transmission
1399 of the “AnTat” seroderme of Trypanosoma brucei. Ann. Soc. Belg. Med. Trop. (1920). *57*.
1400 Rijo-Ferreira, F., Carvalho, T., Afonso, C., Sanches-Vaz, M., Costa, R.M., Figueiredo,
1401 L.M., and Takahashi, J.S. (2018). Sleeping sickness is a circadian disorder. Nat.
1402 Commun. *9*.
1403 Rodgers, J., Bradley, B., Kennedy, P.G.E., and Sternberg, J.M. (2015). Central Nervous
1404 System Parasitosis and Neuroinflammation Ameliorated by Systemic IL-10 Administration
1405 in Trypanosoma brucei-Infected Mice. PLoS Negl. Trop. Dis. *9*, 1–9.
1406 Rojas, F., Silvester, E., Young, J., Smith, T.K., Thompson, J., Matthews, K.R., Rojas, F.,
1407 Silvester, E., Young, J., Milne, R., et al. (2019). Oligopeptide Signaling through Tb GPR89
1408 Drives Trypanosome Quorum Sensing Article Oligopeptide Signaling through Tb GPR89
1409 Drives Trypanosome Quorum Sensing. Cell *176*, 306–317.
1410 Rosser, E.C., and Mauri, C. (2015). Regulatory B Cells: Origin, Phenotype, and Function.
1411 Immunity *42*, 607–612.
1412 Sala Frigerio, C., Wolfs, L., Fattorelli, N., Thrupp, N., Voytyuk, I., Schmidt, I., Mancuso, R.,
1413 Chen, W.T., Woodbury, M.E., Srivastava, G., et al. (2019). The Major Risk Factors for
1414 Alzheimer’s Disease: Age, Sex, and Genes Modulate the Microglia Response to Aβ
1415 Plaques. Cell Rep. *27*, 1293-1306.e6.

1416 Sareneva, T., Matikainen, S., Kurimoto, M., and Julkunen, I. (1998). Influenza A virus-
1417 induced IFN-alpha/beta and IL-18 synergistically enhance IFN-gamma gene expression in
1418 human T cells. J. Immunol. *160*, 6032–6038.
1419 Shao, X., Liao, J., Lu, X., Xue, R., Ai, N., and Fan, X. (2020). scCATCH: Automatic
1420 Annotation on Cell Types of Clusters from Single-Cell RNA Sequencing Data. IScience *23*.
1421 Shemer, A., Scheyltjens, I., Frumer, G.R., Kim, J.S., Grozovski, J., Ayanaw, S., Dassa, B.,
1422 Van Hove, H., Chappell-Maor, L., Boura-Halfon, S., et al. (2020). Interleukin-10 Prevents
1423 Pathological Microglia Hyperactivation following Peripheral Endotoxin Challenge. Immunity
1424 *53*, 1033-1049.e7.
1425 Shi, Y., and Holtzman, D.M. (2018). Interplay between innate immunity and Alzheimer
1426 disease: APOE and TREM2 in the spotlight. Nat. Rev. Immunol. *18*, 759–772.
1427 Smulski, C.R., and Eibel, H. (2018). BAFF and BAFF-receptor in B cell selection and
1428 survival. Front. Immunol. *9*, 1–10.
1429 Spuch, C., Ortolano, S., and Navarro, C. (2012). LRP-1 and LRP-2 receptors function in
1430 the membrane neuron. Trafficking mechanisms and proteolytic processing in alzheimer's
1431 disease. Front. Physiol. *3 JUL*, 1–14.
1432 Stephenson, E., Reynolds, G., Botting, R.A., Calero-Nieto, F.J., Morgan, M.D., Tuong,
1433 Z.K., Bach, K., Sungnak, W., Worlock, K.B., Yoshida, M., et al. (2021). Single-cell multi-
1434 omics analysis of the immune response in COVID-19. Nat. Med. *27*, 904–916.
1435 Strengell, M., Matikainen, S., Sirén, J., Lehtonen, A., Foster, D., Julkunen, I., and
1436 Sareneva, T. (2003). IL-21 in Synergy with IL-15 or IL-18 Enhances IFN-γ Production in
1437 Human NK and T Cells. J. Immunol. *170*, 5464–5469.
1438 Stuart, T., Butler, A., Hoffman, P., Hafemeister, C., Papalexi, E., Mauck, W.M., Hao, Y.,
1439 Stoeckius, M., Smibert, P., and Satija, R. (2019). Comprehensive Integration of Single-Cell
1440 Data. Cell *177*, 1888-1902.e21.
1441 Sun, Y., Ma, J., Li, D., Li, P., Zhou, X., Li, Y., He, Z., Qin, L., Liang, L., and Luo, X. (2019).
1442 Interleukin-10 inhibits interleukin-1β production and inflammasome activation of microglia
1443 in epileptic seizures. J. Neuroinflammation *16*, 1–13.
1444 Szklarczyk, D., Gable, A.L., Lyon, D., Junge, A., Wyder, S., Huerta-Cepas, J., Simonovic,
1445 M., Doncheva, N.T., Morris, J.H., Bork, P., et al. (2019). STRING v11: Protein-protein
1446 association networks with increased coverage, supporting functional discovery in genome-
1447 wide experimental datasets. Nucleic Acids Res. *47*, D607–D613.
1448 Takeda, K., Tsutsui, H., Yoshimoto, T., Adachi, O., Yoshida, N., Kishimoto, T., Okamura,
1449 H., Nakanishi, K., and Akira, S. (1998). Defective NK cell activity and Th1 response in IL-

18-deficient mice. Immunity *8*, 383–390.

Tesoriero, C., Xu, Y.Z., Mumba Ngoyi, D., and Bentivoglio, M. (2018). Neural damage in experimental trypanosoma brucei gambiense infection: The suprachiasmatic nucleus. Front. Neuroanat. *12*, 1–10.

Vaeth, M., Wang, Y.H., Eckstein, M., Yang, J., Silverman, G.J., Lacruz, R.S., Kannan, K., and Feske, S. (2019). Tissue resident and follicular Treg cell differentiation is regulated by CRAC channels. Nat. Commun. *10*.

Wang, H. (2021). Microglia Heterogeneity in Alzheimer's Disease: Insights From Single-Cell Technologies. Front. Synaptic Neurosci. *13*, 1–10.

Wang, P., Yao, L., Luo, M., Zhou, W., Jin, X., Xu, Z., Yan, S., Li, Y., Xu, C., Cheng, R., et al. (2021a). Single-cell transcriptome and TCR profiling reveal activated and expanded T cell populations in Parkinson's disease. Cell Discov. *7*.

Wang, Y., Chen, D., Xu, D., Huang, C., Xing, R., He, D., and Xu, H. (2021b). Early developing B cells undergo negative selection by central nervous system-specific antigens in the meninges. Immunity *54*, 2784-2794.e6.

Watanabe, S., Alexander, M., Misharin, A. V., and Budinger, G.R.S. (2019). The role of macrophages in the resolution of inflammation. J. Clin. Invest. *129*, 2619–2628.

Wickham, H. (2016). ggplot2: Elegant Graphics for Data Analysis. Springer-Verlag New York.

Wickham, H., François, R., Henry, L., and Müller, K. (2022). dplyr: A Grammar of Data Manipulation.

Wollenberg, I., Agua-Doce, A., Hernández, A., Almeida, C., Oliveira, V.G., Faro, J., and Graca, L. (2011). Regulation of the Germinal Center Reaction by Foxp3 + Follicular Regulatory T Cells . J. Immunol. *187*, 4553–4560.

Wynn, T.A., and Vannella, K.M. (2016). Macrophages in Tissue Repair, Regeneration, and Fibrosis. Immunity *44*, 450–462.

Figure 1

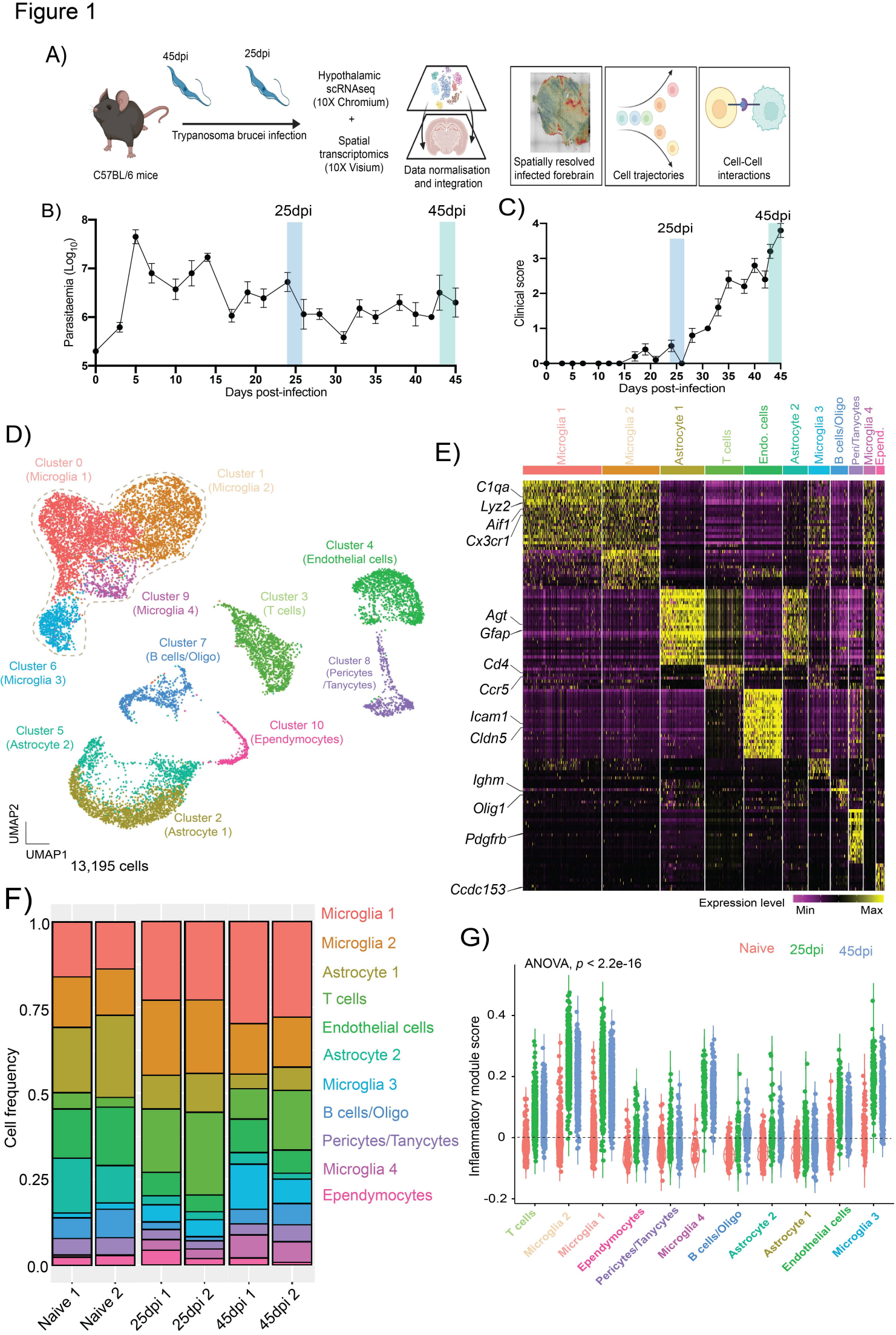
A)
45dpi
25dpi
C57BL/6 mice
Trypanosoma brucei infection
Hypothalamic scRNAseq (10X Chromium)
+
Spatial transcriptomics (10X Visium)
Data normalisation and integration
Spatially resolved infected forebrain
Cell trajectories
Cell-Cell interactions
B)
25dpi
45dpi
Parasitaemia (Log10)
Days post-infection
C)
25dpi
45dpi
Clinical score
Days post-infection
D)
Cluster 0 (Microglia 1)
Cluster 1 (Microglia 2)
Cluster 4 (Endothelial cells)
Cluster 9 (Microglia 4)
Cluster 3 (T cells)
Cluster 7 (B cells/Oligo)
Cluster 6 (Microglia 3)
Cluster 8 (Pericytes /Tanycytes)
Cluster 10 (Ependymocytes)
Cluster 5 (Astrocyte 2)
Cluster 2 (Astrocyte 1)
UMAP2
UMAP1
13,195 cells
E)
Microglia 1
Microglia 2
Astrocyte 1
T cells
Endo. cells
Astrocyte 2
Microglia 3
B cells/Oligo
Peri/Tanycytes
Microglia 4
Ependy.
C1qa
Lyz2
Aif1
Cx3cr1
Agt
Gfap
Cd4
Ccr5
Icam1
Cldn5
Ighm
Olig1
Pdgfrb
Ccdc153
Expression level
Min
Max
F)
Cell frequency
Naive 1
Naive 2
25dpi 1
25dpi 2
45dpi 1
45dpi 2
Microglia 1
Microglia 2
Astrocyte 1
T cells
Endothelial cells
Astrocyte 2
Microglia 3
B cells/Oligo
Pericytes/Tanycytes
Microglia 4
Ependymocytes
G)
ANOVA, p < 2.2e-16
Naive
25dpi
45dpi
Inflammatory module score
T cells
Microglia 2
Microglia 1
Ependymocytes
Pericytes/Tanycytes
Microglia 4
B cells/Oligo
Astrocyte 2
Astrocyte 1
Endothelial cells
Microglia 3

Figure 2

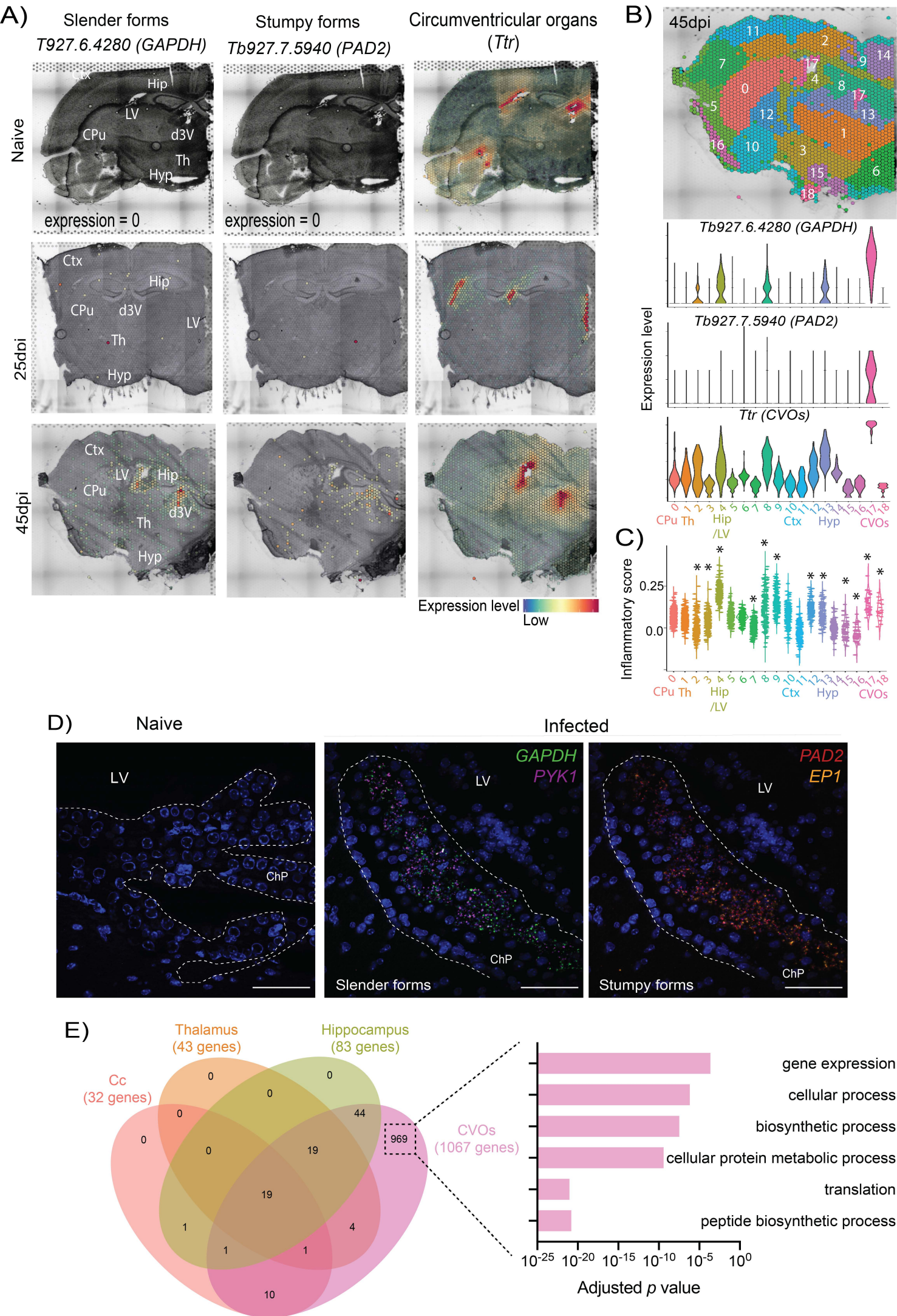
A)
Slender forms
T927.6.4280 (GAPDH)
Stumpy forms
Tb927.7.5940 (PAD2)
Circumventricular organs
(Ttr)
Naive
25dpi
45dpi
Ctx
Hip
LV
CPu
d3V
Th
Hyp
expression = 0
Expression level
Low
B)
45dpi
Tb927.6.4280 (GAPDH)
Tb927.7.5940 (PAD2)
Ttr (CVOs)
Expression level
CPu Th Hip /LV Ctx Hyp CVOs
C)
Inflammatory score
0.25
0.0
CPu Th Hip /LV Ctx Hyp CVOs
D)
Naive
Infected
LV
ChP
GAPDH
PYK1
PAD2
EP1
Slender forms
Stumpy forms
E)
Thalamus
(43 genes)
Hippocampus
(83 genes)
Cc
(32 genes)
CVOs
(1067 genes)
969
gene expression
cellular process
biosynthetic process
cellular protein metabolic process
translation
peptide biosynthetic process
Adjusted p value

Figure 3

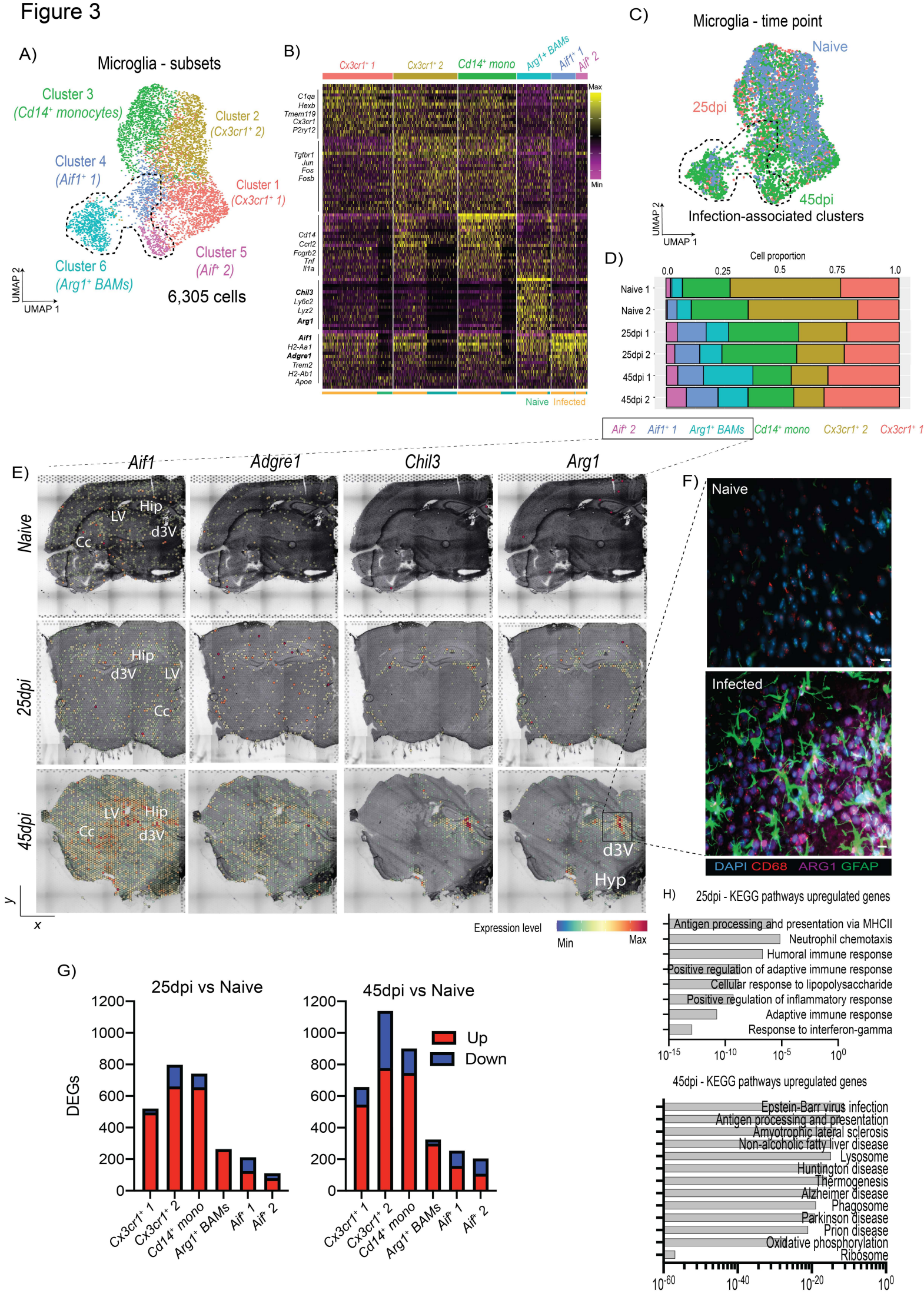
A)
Microglia - subsets
Cluster 3 (Cd14+ monocytes)
Cluster 2 (Cx3cr1+ 2)
Cluster 4 (Aif1+ 1)
Cluster 1 (Cx3cr1+ 1)
Cluster 5 (Aif+ 2)
Cluster 6 (Arg1+ BAMs)
6,305 cells
UMAP 2
UMAP 1
B)
Cx3cr1+ 1
Cx3cr1+ 2
Cd14+ mono
Arg1+ BAMs
Aif1+ 1
Aif+ 2
Max
Min
C1qa
Hexb
Tmem119
Cx3cr1
P2ry12
Tgfbr1
Jun
Fos
Fosb
Cd14
Ccrl2
Fcgrb2
Tnf
Il1a
Chil3
Ly6c2
Lyz2
Arg1
Aif1
H2-Aa1
Adgre1
Trem2
H2-Ab1
Apoe
Naive
Infected
C)
Microglia - time point
Naive
25dpi
45dpi
Infection-associated clusters
UMAP 2
UMAP 1
D)
Cell proportion
0.0
0.25
0.5
0.75
1.0
Naive 1
Naive 2
25dpi 1
25dpi 2
45dpi 1
45dpi 2
Aif+ 2
Aif1+ 1
Arg1+ BAMs
Cd14+ mono
Cx3cr1+ 2
Cx3cr1+ 1
E)
Aif1
Adgre1
Chil3
Arg1
Naive
25dpi
45dpi
Hip
LV
d3V
Cc
Hyp
y
x
Expression level
Min
Max
F)
Naive
Infected
DAPI CD68 ARG1 GFAP
H)
25dpi - KEGG pathways upregulated genes
Antigen processing and presentation via MHCII
Neutrophil chemotaxis
Humoral immune response
Positive regulation of adaptive immune response
Cellular response to lipopolysaccharide
Positive regulation of inflammatory response
Adaptive immune response
Response to interferon-gamma
10-15
10-10
10-5
100
45dpi - KEGG pathways upregulated genes
Epstein-Barr virus infection
Antigen processing and presentation
Amyotrophic lateral sclerosis
Non-alcoholic fatty liver disease
Lysosome
Huntington disease
Thermogenesis
Alzheimer disease
Phagosome
Parkinson disease
Prion disease
Oxidative phosphorylation
Ribosome
10-60
10-40
10-20
100
G)
25dpi vs Naive
45dpi vs Naive
DEGs
1200
1000
800
600
400
200
0
Up
Down
Cx3cr1+ 1
Cx3cr1+ 2
Cd14+ mono
Arg1+ BAMs
Aif+ 1
Aif+ 2

Figure 4

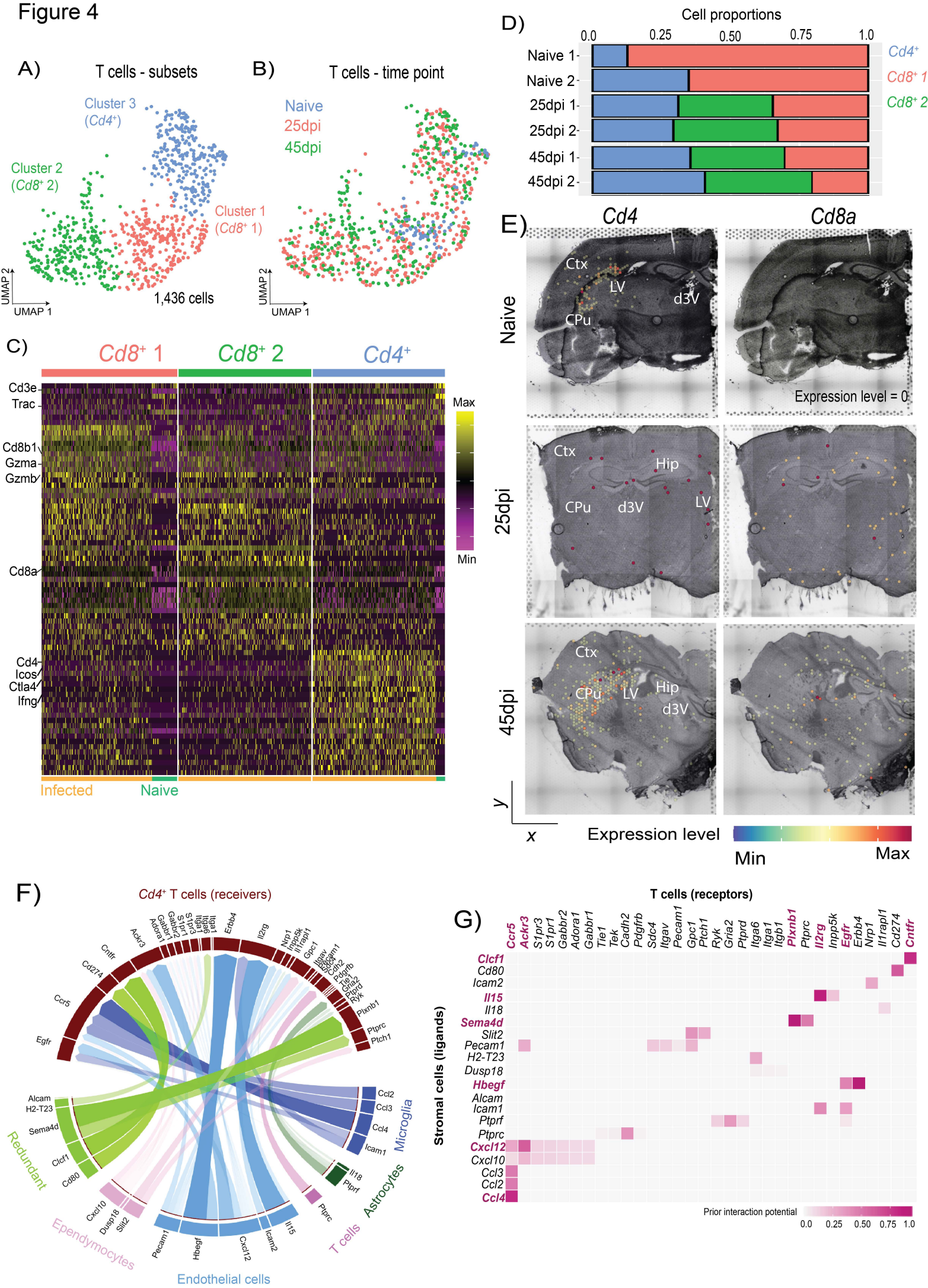
A)
T cells - subsets
Cluster 3 (Cd4+)
Cluster 2 (Cd8+ 2)
Cluster 1 (Cd8+ 1)
1,436 cells
UMAP 2
UMAP 1
B)
T cells - time point
Naive
25dpi
45dpi
UMAP 2
UMAP 1
C)
Cd8+ 1
Cd8+ 2
Cd4+
Cd3e
Trac
Cd8b1
Gzma
Gzmb
Cd8a
Cd4
Icos
Ctla4
Ifng
Max
Min
Infected
Naive
D)
Cell proportions
0.0
0.25
0.50
0.75
1.0
Naive 1
Naive 2
25dpi 1
25dpi 2
45dpi 1
45dpi 2
Cd4+
Cd8+ 1
Cd8+ 2
E)
Cd4
Cd8a
Naive
25dpi
45dpi
Ctx
LV
d3V
CPu
Hip
Expression level = 0
y
x
Expression level
Min
Max
F)
Cd4+ T cells (receivers)
Cntfr
Cd274
Ccr5
Egfr
Ackr3
Adora1
Gabbr1
Gabbr2
S1pr1
S1pr3
Tie1
Tek
Erbb4
Il2rg
Nrp1
Inpp5k
Il1rapl1
Gpc1
Itgav
Pecam1
Sdc4
Cdh2
Pdgfrb
Tlr1
Gria2
Ptprd
Ryk
Plxnb1
Ptprc
Ptch1
Alcam
H2-T23
Sema4d
Clcf1
Cd80
Cxcl10
Dusp18
Slit2
Pecam1
Hbegf
Cxcl12
Icam2
Il15
Ptprc
Il18
Ptprf
Ccl2
Ccl3
Ccl4
Icam1
Redundant
Ependymocytes
Endothelial cells
T cells
Astrocytes
Microglia
G)
T cells (receptors)
Stromal cells (ligands)
Ccr5
Ackr3
S1pr3
S1pr1
Gabbr2
Adora1
Gabbr1
Tie1
Tek
Cadh2
Pdgfrb
Sdc4
Itgav
Pecam1
Gpc1
Ptch1
Ryk
Gria2
Ptprd
Itga6
Itga1
Itgb1
Plxnb1
Ptprc
Il2rg
Inpp5k
Egfr
Erbb4
Nrp1
Il1rapl1
Cd274
Cntfr
Clcf1
Cd80
Icam2
Il15
Il18
Sema4d
Slit2
Pecam1
H2-T23
Dusp18
Hbegf
Alcam
Icam1
Ptprf
Ptprc
Cxcl12
Cxcl10
Ccl3
Ccl2
Ccl4
Prior interaction potential
0.0
0.25
0.50
0.75
1.0

Figure 5

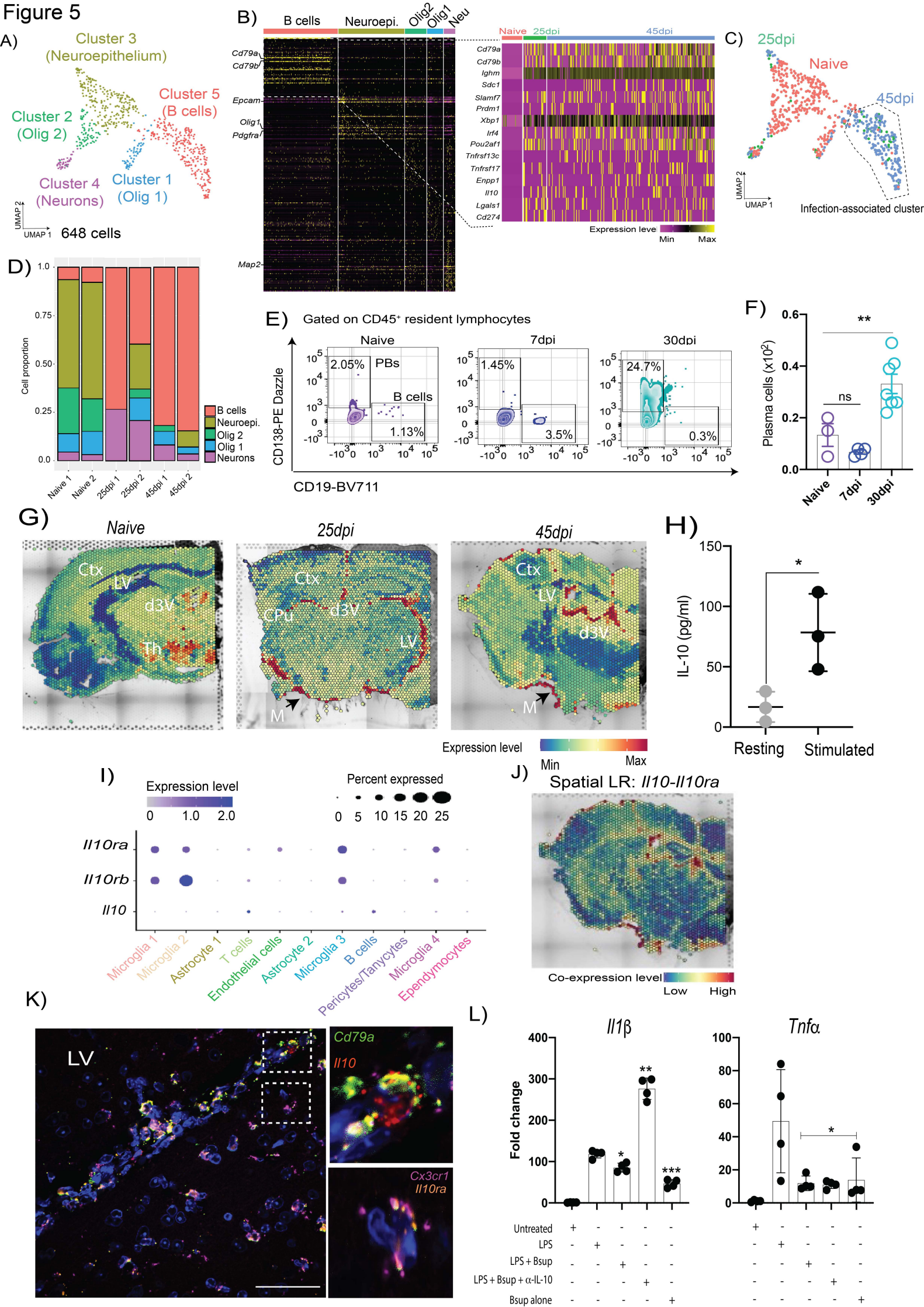
A)
Cluster 3 (Neuroepithelium)
Cluster 5 (B cells)
Cluster 2 (Olig 2)
Cluster 4 (Neurons)
Cluster 1 (Olig 1)
UMAP 2
UMAP 1
648 cells
B)
B cells
Neuroepi.
Olig2
Olig1
Neu
Cd79a
Cd79b
Epcam
Olig1
Pdgfra
Map2
Naive
25dpi
45dpi
Cd79a
Cd79b
Ighm
Sdc1
Slamf7
Prdm1
Xbp1
Irf4
Pou2af1
Tnfrsf13c
Tnfrsf17
Enpp1
Il10
Lgals1
Cd274
Expression leve
Min
Max
C)
25dpi
Naive
45dpi
UMAP 2
UMAP 1
Infection-associated cluster
D)
Cell proportion
1.0
0.75
0.50
0.25
0.0
B cells
Neuroepi.
Olig 2
Olig 1
Neurons
Naive 1
Naive 2
25dpi 1
25dpi 2
45dpi 1
45dpi 2
E)
Gated on CD45⁺ resident lymphocytes
Naive
7dpi
30dpi
CD138-PE Dazzle
CD19-BV711
2.05%
PBs
B cells
1.13%
1.45%
3.5%
24.7%
0.3%
F)
Plasma cells (x10²)
**
ns
Naive
7dpi
30dpi
G)
Naive
25dpi
45dpi
Ctx
LV
d3V
Th
CPu
M
Expression level
Min
Max
H)
IL-10 (pg/ml)
*
Resting
Stimulated
I)
Expression level
0
1.0
2.0
Percent expressed
0
5
10
15
20
25
Il10ra
Il10rb
Il10
Microglia 1
Microglia 2
Astrocyte 1
T cells
Endothelial cells
Astrocyte 2
Microglia 3
B cells
Pericytes/Tanycytes
Microglia 4
Ependymocytes
J)
Spatial LR: Il10-Il10ra
Co-expression level
Low
High
K)
LV
Cd79a
Il10
Cx3cr1
Il10ra
L)
Il1β
Tnfα
Fold change
**
*
***
Untreated
LPS
LPS + Bsup
LPS + Bsup + α-IL-10
Bsup alone

Figure 6

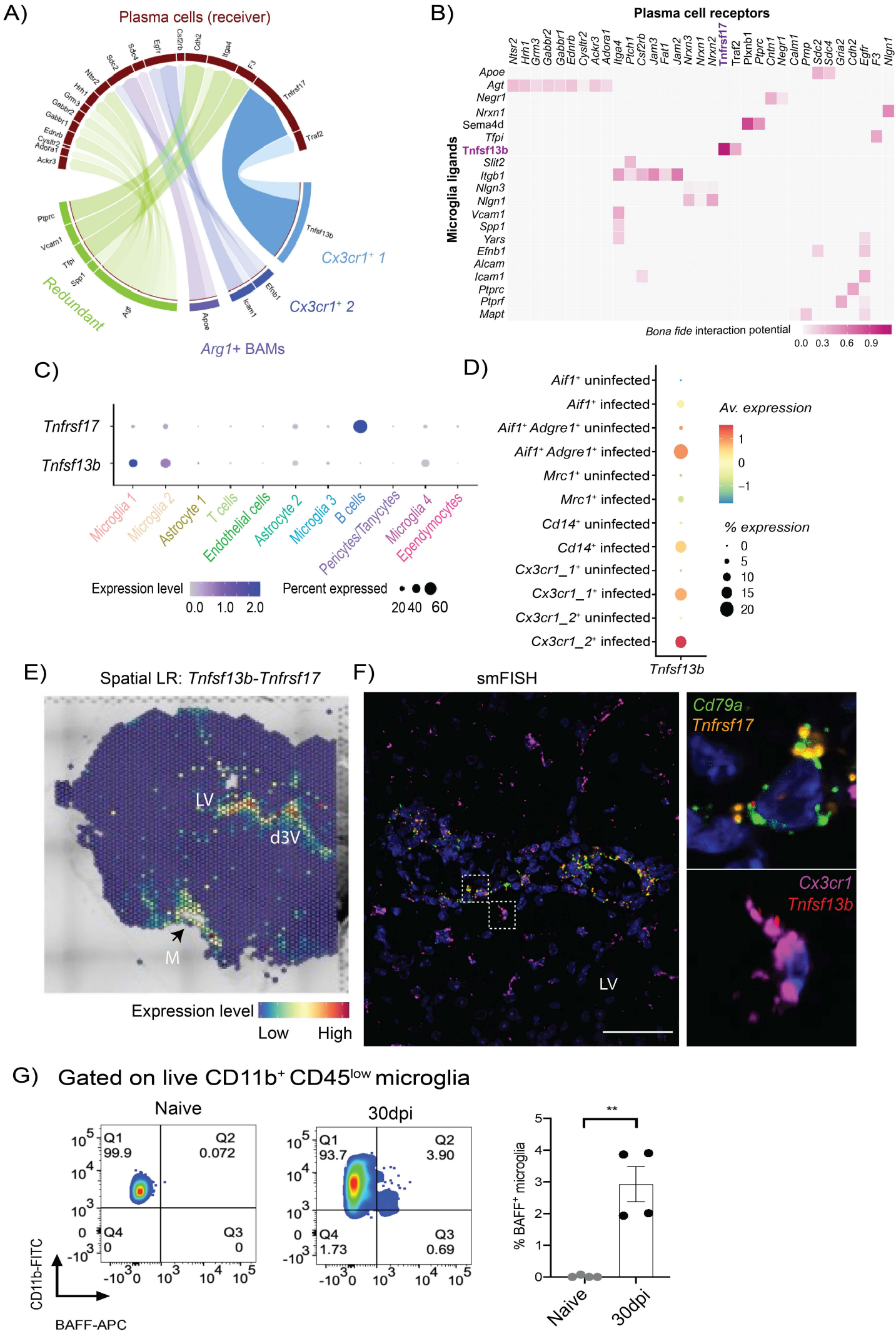
A)
Plasma cells (receiver)
Ntsr2
Hrh1
Grm3
Gabbr2
Gabbr1
Ednrb
Cysltr2
Adora1
Ackr3
Sdc2
Sdc4
Egfr
Csf2rb
Cdh2
Itga4
F3
Tnfrsf17
Traf2
Tnfsf13b
Cx3cr1+ 1
Cx3cr1+ 2
Efnb1
Icam1
Apoe
Agt
Spp1
Tfpi
Vcam1
Ptprc
Redundant
Arg1+ BAMs
B)
Plasma cell receptors
Ntsr2
Hrh1
Grm3
Gabbr2
Gabbr1
Ednrb
Cysltr2
Ackr3
Adora1
Itga4
Ptch1
Csf2rb
Jam3
Fat1
Jam2
Nrxn3
Nrxn1
Nrxn2
Tnfrsf17
Traf2
Plxnb1
Ptprc
Cntn1
Negr1
Calm1
Pmp
Sdc2
Sdc4
Gria2
Cdh2
Egfr
F3
Nlgn1
Microglia ligands
Apoe
Agt
Negr1
Nrxn1
Sema4d
Tfpi
Tnfsf13b
Slit2
Itgb1
Nlgn3
Nlgn1
Vcam1
Spp1
Yars
Efnb1
Alcam
Icam1
Ptprc
Ptprf
Mapt
Bona fide interaction potential
0.0 0.3 0.6 0.9
C)
Tnfrsf17
Tnfsf13b
Microglia 1
Microglia 2
Astrocyte 1
T cells
Endothelial cells
Astrocyte 2
Microglia 3
B cells
Pericytes/Tanycytes
Microglia 4
Ependymocytes
Expression level
0.0 1.0 2.0
Percent expressed
20 40 60
D)
Aif1+ uninfected
Aif1+ infected
Aif1+ Adgre1+ uninfected
Aif1+ Adgre1+ infected
Mrc1+ uninfected
Mrc1+ infected
Cd14+ uninfected
Cd14+ infected
Cx3cr1_1+ uninfected
Cx3cr1_1+ infected
Cx3cr1_2+ uninfected
Cx3cr1_2+ infected
Tnfsf13b
Av. expression
1
0
−1
% expression
0
5
10
15
20
E)
Spatial LR: Tnfsf13b-Tnfrsf17
LV
d3V
M
Expression level
Low
High
F)
smFISH
LV
Cd79a
Tnfrsf17
Cx3cr1
Tnfsf13b
G)
Gated on live CD11b+ CD45low microglia
Naive
Q1
99.9
Q2
0.072
Q4
0
Q3
0
30dpi
Q1
93.7
Q2
3.90
Q4
1.73
Q3
0.69
CD11b-FITC
BAFF-APC
% BAFF+ microglia
**
Naive
30dpi

Figure S1

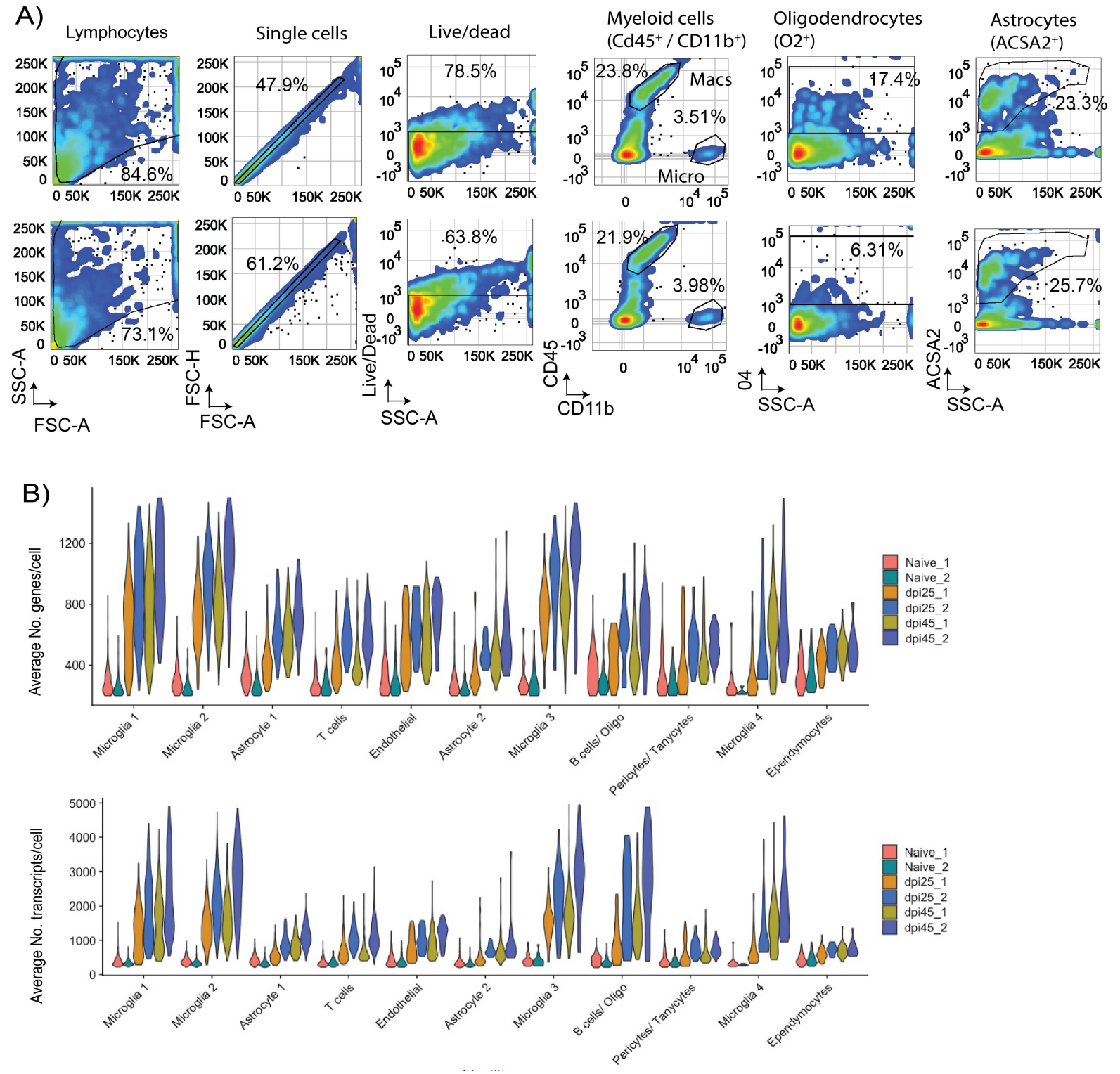
A)
Lymphocytes
Single cells
Live/dead
Myeloid cells (Cd45+ / CD11b+)
Oligodendrocytes (O2+)
Astrocytes (ACSA2+)
84.6%
73.1%
47.9%
61.2%
78.5%
63.8%
23.8%
Macs
3.51%
Micro
21.9%
3.98%
17.4%
6.31%
23.3%
25.7%
SSC-A
FSC-A
FSC-H
Live/Dead
CD45
CD11b
O4
ACSA2
B)
Average No. genes/cell
Average No. transcripts/cell
Naive_1
Naive_2
dpi25_1
dpi25_2
dpi45_1
dpi45_2
Microglia 1
Microglia 2
Astrocyte 1
T cells
Endothelial
Astrocyte 2
Microglia 3
B cells/ Oligo
Pericytes/ Tanycytes
Microglia 4
Ependymocytes
C)
Lymphocytes
Singlets
Live cells
Resident vs circulating CD45+ cells
36.7%
69.3%
79.2%
Circulating 2.5%
Resident 97.5%
Live-dead
CD45 (PE)
CD45 (BV421)

Figure S2

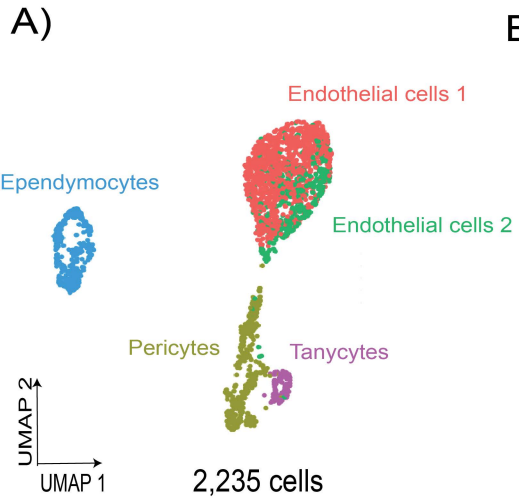

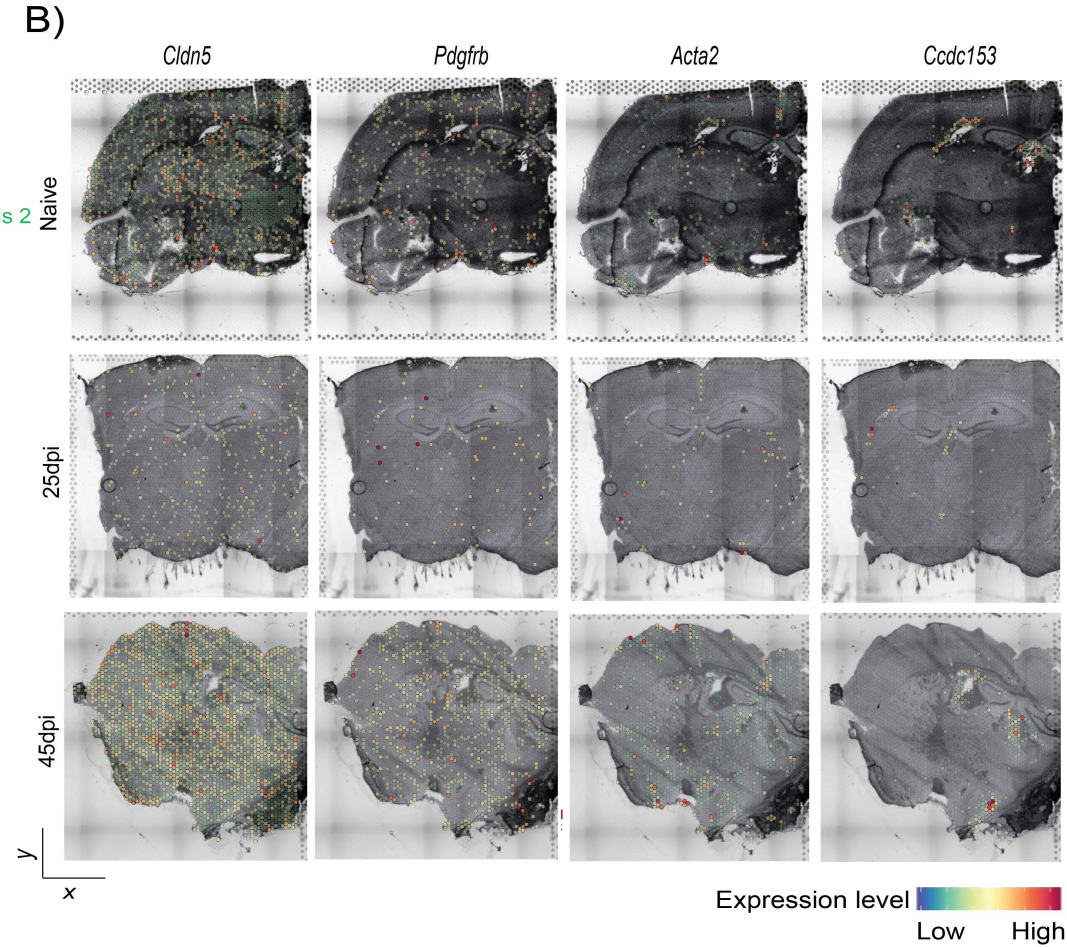

Figure 2

Figure S3

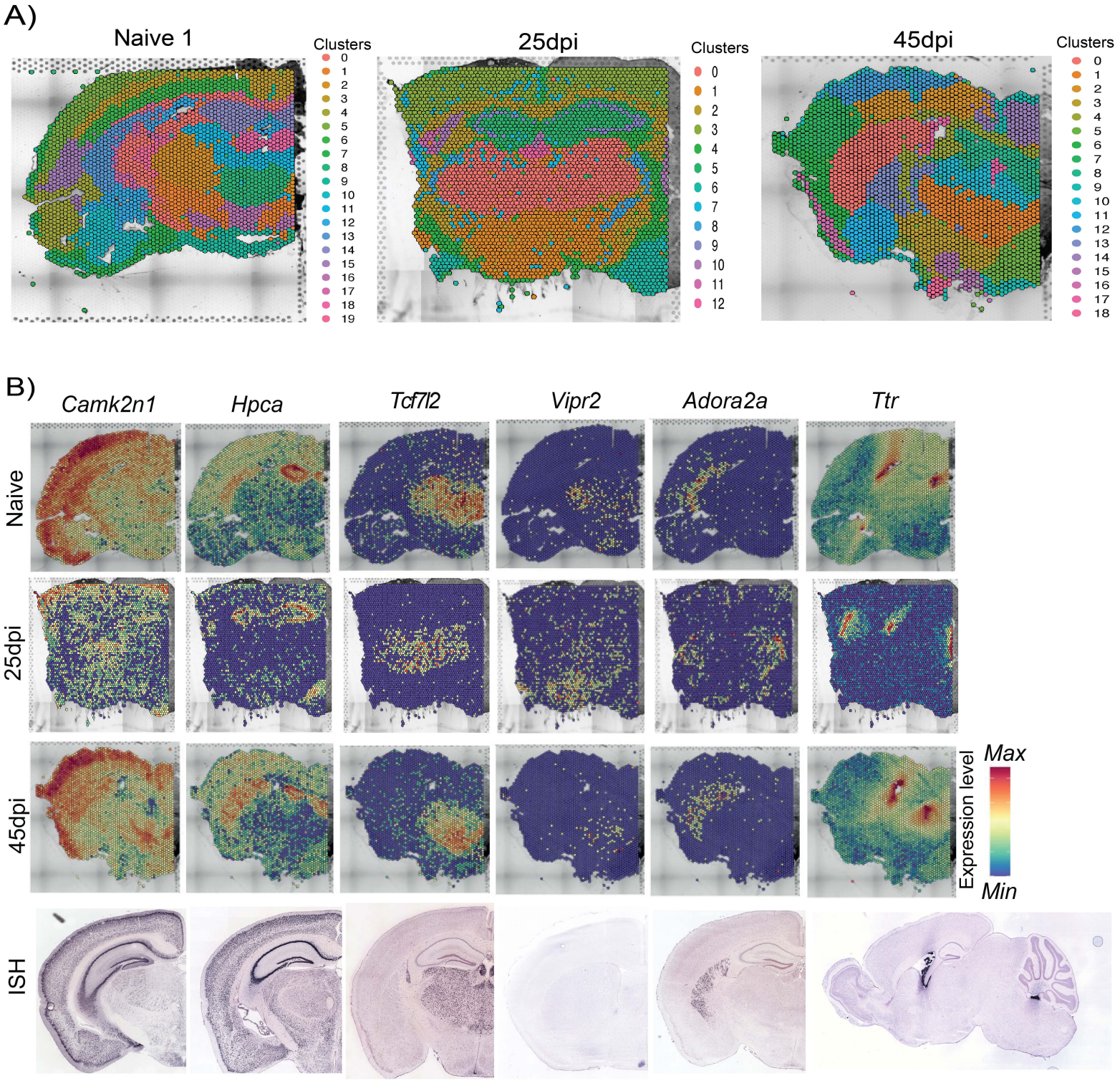
A)
Naive 1
Clusters
0 1 2 3 4 5 6 7 8 9 10 11 12 13 14 15 16 17 18 19
25dpi
Clusters
0 1 2 3 4 5 6 7 8 9 10 11 12
45dpi
Clusters
0 1 2 3 4 5 6 7 8 9 10 11 12 13 14 15 16 17 18
B)
Camk2n1
Hpca
Tcf7l2
Vipr2
Adora2a
Ttr
Naive
25dpi
45dpi
ISH
Max
Expression level
Min

Figure S4

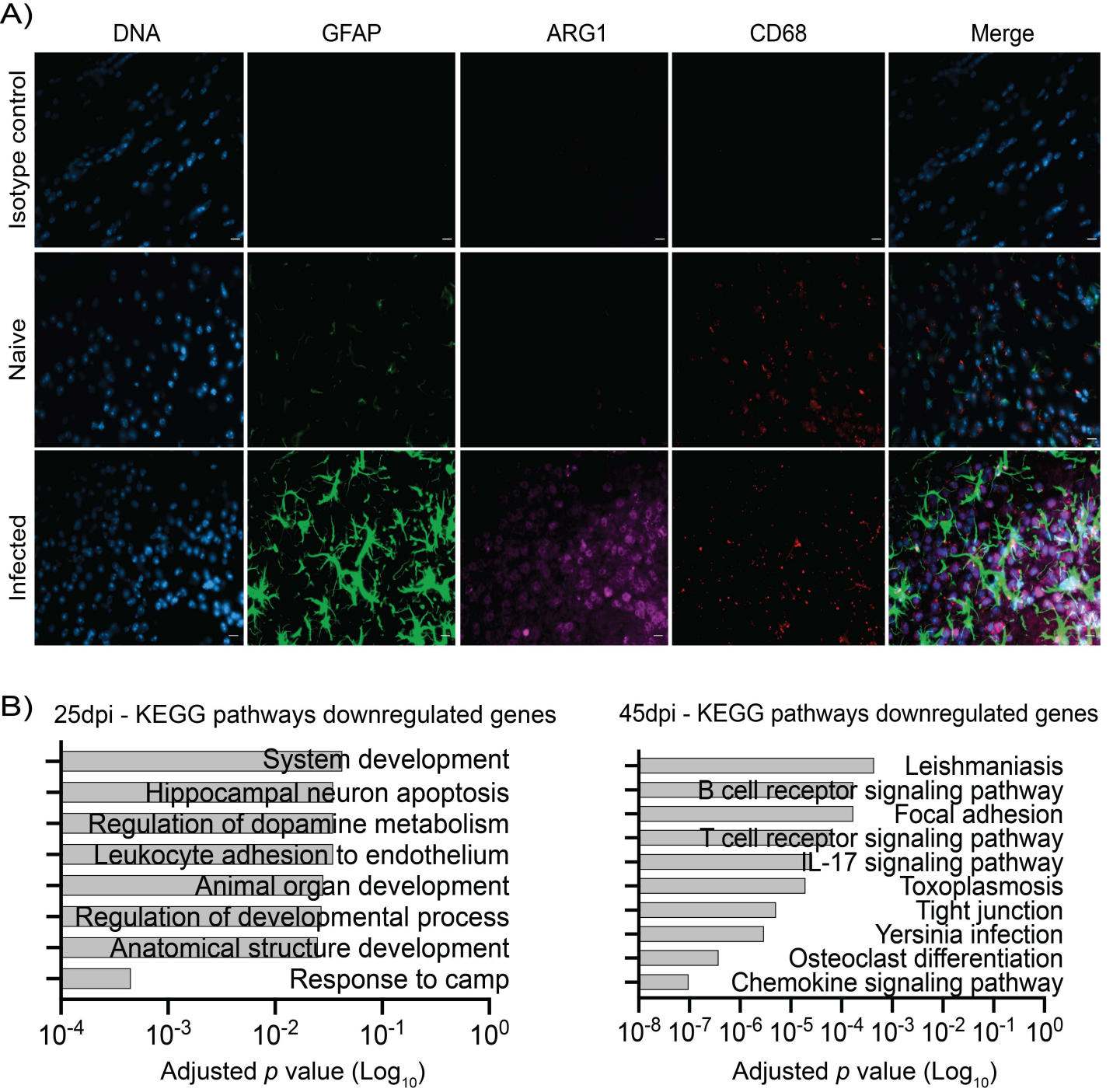
A)
DNA
GFAP
ARG1
CD68
Merge
Isotype control
Naive
Infected
B)
25dpi - KEGG pathways downregulated genes
System development
Hippocampal neuron apoptosis
Regulation of dopamine metabolism
Leukocyte adhesion to endothelium
Animal organ development
Regulation of developmental process
Anatomical structure development
Response to camp
10^{-4} 10^{-3} 10^{-2} 10^{-1} 10^{0}
Adjusted *p* value (Log_{10})
45dpi - KEGG pathways downregulated genes
Leishmaniasis
B cell receptor signaling pathway
Focal adhesion
T cell receptor signaling pathway
IL-17 signaling pathway
Toxoplasmosis
Tight junction
Yersinia infection
Osteoclast differentiation
Chemokine signaling pathway
10^{-8} 10^{-7} 10^{-6} 10^{-5} 10^{-4} 10^{-3} 10^{-2} 10^{-1} 10^{0}
Adjusted *p* value (Log_{10})

Figure S5

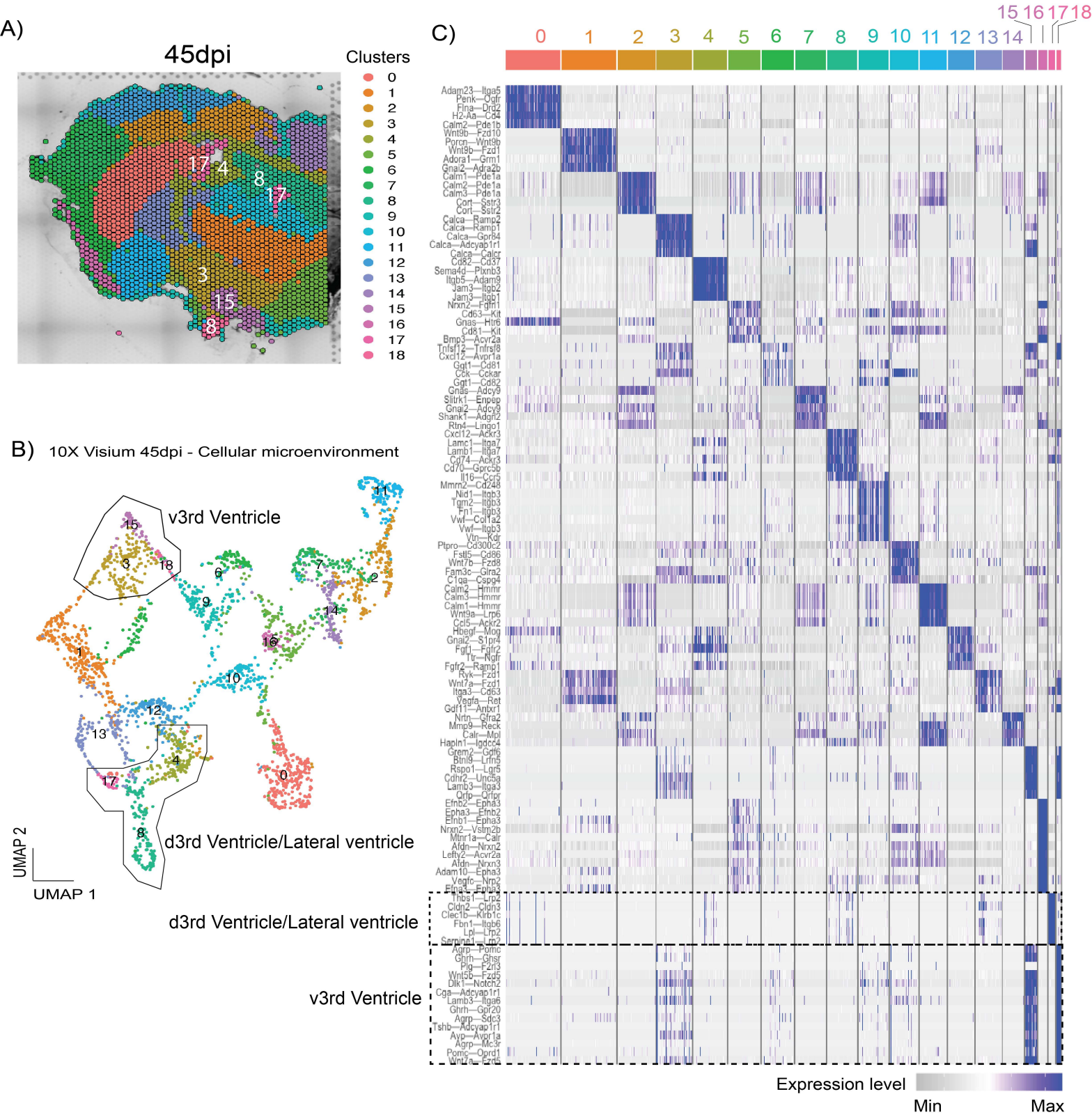
A)
45dpi
Clusters
0
1
2
3
4
5
6
7
8
9
10
11
12
13
14
15
16
17
18
B)
10X Visium 45dpi - Cellular microenvironment
v3rd Ventricle
d3rd Ventricle/Lateral ventricle
UMAP 2
UMAP 1
C)
d3rd Ventricle/Lateral ventricle
v3rd Ventricle
Expression level
Min
Max

Figure S6

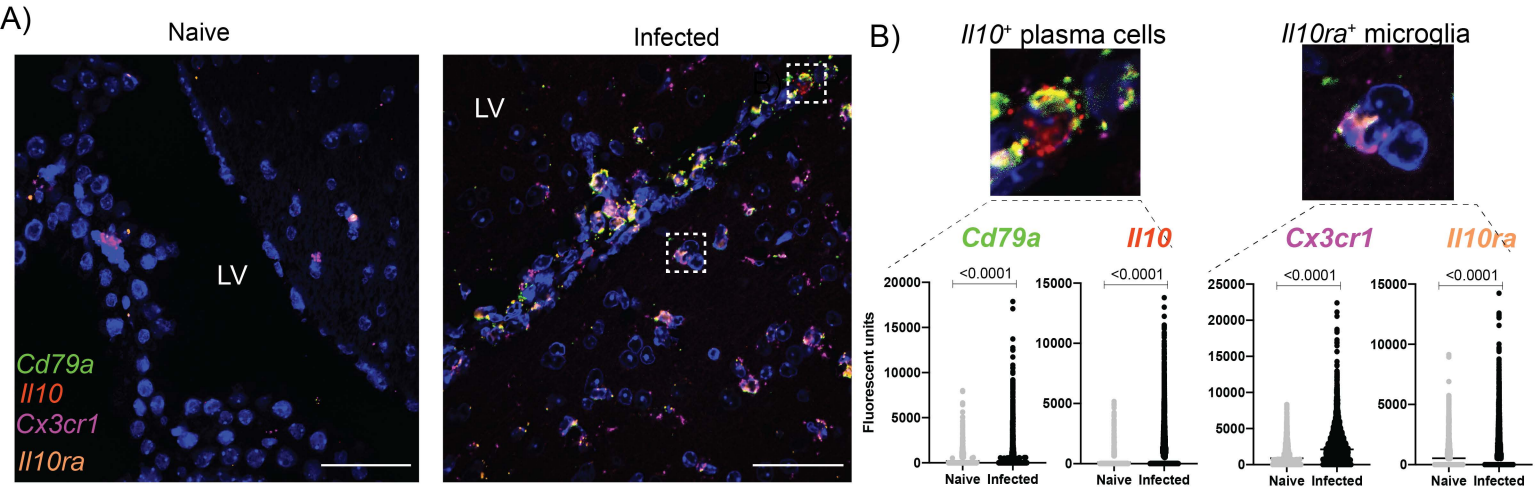
A)
Naive
Infected
LV
LV
Cd79a
Il10
Cx3cr1
Il10ra
B)
Il10+ plasma cells
Il10ra+ microglia
Cd79a
Il10
Cx3cr1
Il10ra
<0.0001
Fluorescent units
Naive
Infected

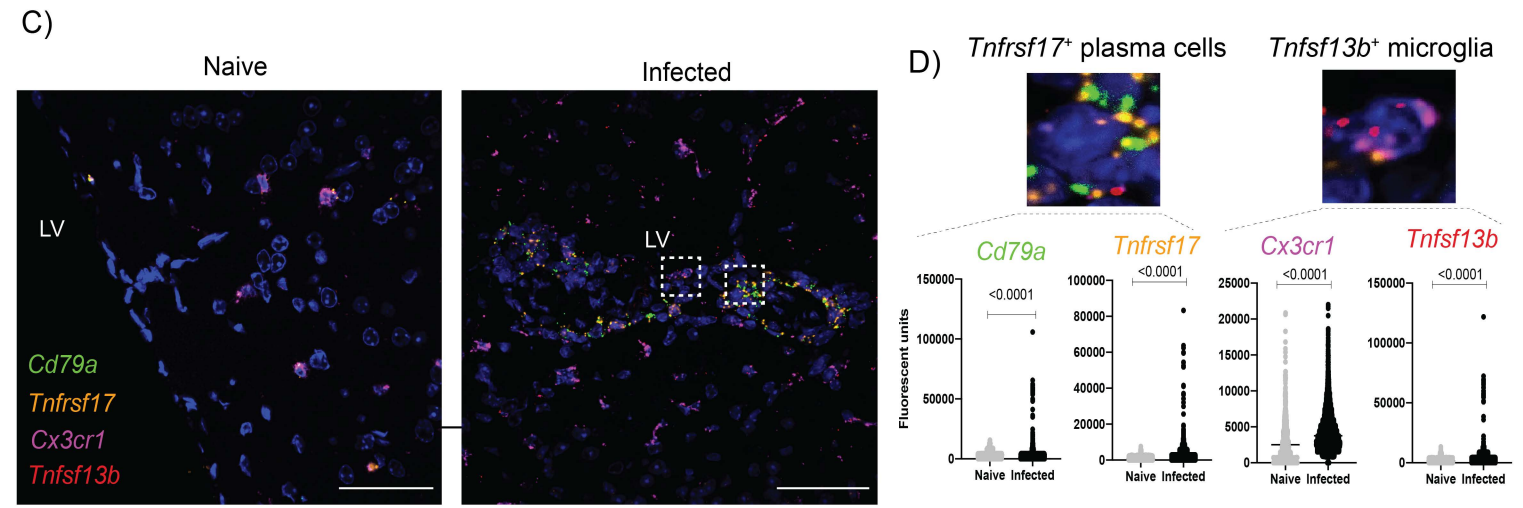
C)
Naive
Infected
LV
LV
Cd79a
Tnfrsf17
Cx3cr1
Tnfsf13b
D)
Tnfrsf17+ plasma cells
Tnfsf13b+ microglia
Cd79a
Tnfrsf17
Cx3cr1
Tnfsf13b
<0.0001
Fluorescent units
Naive
Infected

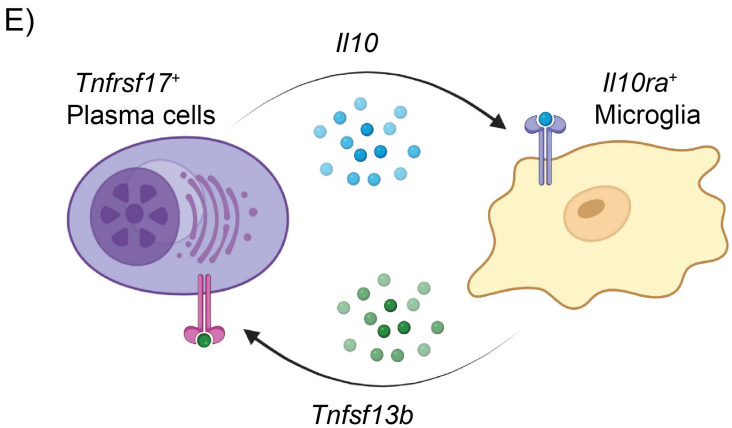
E)
Tnfrsf17+
Plasma cells
Il10
Il10ra+
Microglia
Tnfsf13b